Complex blood flow patterns in an idealized left ventricle: a numerical study

Tagliabue, A; Dede', L.; Quarteroni A.

MOX, Dipartimento di Matematica
Politecnico di Milano, Via Bonardi 9 - 20133 Milano (Italy)

mox-dmat@polimi.it   http://mox.polimi.it

Complex blood flow patterns in an idealized left ventricle: a numerical study.

Anna Tagliabue [1,2,*], Luca Dedè [1], and Alfio Quarteroni [1,2,†]

[1] CMCS – Chair of Modeling and Scientific Computing
MATHICSE – Mathematics Institute of Computational Science and Engineering
EPFL – École Polytechnique Fédérale de Lausanne
Station 8, Lausanne, CH – 1015, Switzerland

[2] MOX–Modeling and Scientific Computing,
Mathematics Department "F. Brioschi",
Politecnico di Milano, via Bonardi 9, Milano, 20133, Italy

Abstract

In this paper, we study the blood flow dynamics in a three-dimensional (3D) idealized left ventricle of the human heart whose deformation is driven by muscle contraction and relaxation in coordination with the action of the mitral and aortic valves. We propose a simplified but realistic mathematical treatment of the valves function based on mixed time-varying boundary conditions (BCs) for the Navier-Stokes equations modeling the flow. These switching in time BCs, from natural to essential and viceversa, model either the open or the closed configurations of the valves. At the numerical level these BCs are enforced by means of the extended Nitsche's method [A. Tagliabue et al., MATHICSE report, 2015]. Numerical results for 3D idealized left ventricle obtained by means of Isogeometric Analysis are presented, discussed in terms of both instantaneous and phase-averaged quantities of interest and validated against those available in literature, both experimental and computational. The complex blood flow patterns are analysed to describe the characteristic fluid properties, to show the transitional nature of the flow, and to highlight its main features inside the left ventricle. The sensitivity of the intraventricular flow patterns to the mitral valve properties is also investigated.

Key words. heart modeling; fluid dynamics; mixed time-varying boundary conditions; extended Nitsche's method; Isogeometric Analysis; left ventricle; valves modeling.

---

*Corresponding author. E-mail: anna.tagliabue@epfl.ch. Phone: +41 21 69 30359.
†Currently on leave from Politecnico di Milano.

1   Introduction

In the last decades, several studies have been performed to understand and describe the morphology and functioning of the heart through numerical simulations; see e.g. [66] for an overview. Focusing, specifically, on the left ventricle (LV) – which plays a fundamental role in the cardiac activity by distributing oxygenated blood to the body through the aorta – growing attention has been dedicated to the blood flow dynamics. This is also made possible by the recent technological advances in medical imaging techniques [71], e.g. phase-contrast magnetic resonance imaging [50, 47] and echocardiography [38, 49]. However, these techniques still present some drawbacks as e.g. a relatively poor spatio-temporal resolution, which prevents the analysis of small-scale instabilities and locally fast flow variations, the presence of aliasing artefacts and the output of phase averaged flows quantities, which neglect beat to beat variations [16].

Mathematical and computational models assume a relevant role in providing accurate descriptions of the blood flow features and in performing simulations in both idealized configurations [2, 3, 23, 24, 25] or in subject-specific cardiac geometries [16, 82]. Several challenges arise. The LV chamber has a complex shape; moreover, it expands and contracts by experiencing large displacements driven by a complex electrical-fluid-structure interaction mechanism. The blood flow, mainly regulated by the action of the valves, features different regimes, varying along the heartbeat from laminar to transitional, and eventually turbulent. Because of these aspects and the general lack of accurate clinical data describing e.g. the mechanical properties of the wall or the blood flow profile through the mitral valve, several simplifying assumptions need often to be made.

In this work, we present a numerical study of the hemodynamics inside the LV by considering an idealized geometry represented by a truncate prolate ellipsoid, which is considered in literature [2, 3] as sufficiently accurate to represent the average endocardial shape of different human subjects. Moreover, the motion of the LV cavity, which is completely characterized by the time variations of the upper diameter and of the major semi-axis of the ellipsoid, is prescribed by a wall law derived from a simple elastic model coupled to a flow-discharge function, in the framework of [2, 3]. Our model focuses on a simplified but realistic treatment of the valves, which are considered as orifices of infinitesimal thickness located on the boundary of the LV domain. Due to their role in regulating the flow inside the LV and to their strong influence on it, several models have been proposed in literature to account for the valves in a realistic and physiologically meaningful manner. In particular, the valves are modeled as immersed surfaces in the fluid either in a restricted area near the valves [31, 40, 42, 53] or in full left heart models [1, 16]. In this work, following [76], we model the valves function as boundary conditions (BCs) for the Navier-Stokes equations which mathematically describe the blood flow by considering a 3D LV chamber with the valves located on its boundary. This leads to some mathematical and numerical challenges, since the open and closed configurations of the valves involve the treatment of BCs switching from essential to natural and viceversa during the heartbeat. We use mixed time-varying (MTV) BCs for the Navier-Stokes equations in the Arbitrary Lagrangian Eulerian (ALE) formulation and we embed them in the variational formulation of the problem in the framework of the extended Nitsche's method (ENM), as done in [76] for a two-dimensional problem. By using our method, the Galerkin formulation of the problem involves time independent function spaces, the switching in time between the Dirichlet and defective BCs of natural type is straightforward, and the imposition of the boundary data is fulfilled by using a penalty technique.

In order to asses the capability of our valves modelling approach, we numerically compute the
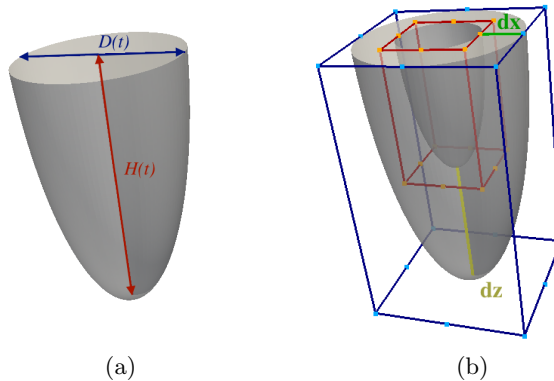
Figure 1: 3D idealized human LV (a); geometric construction of the LV from the NURBS volumetric geometry (b) with control points in blue (▪) and orange (▪).

3D blood flow in an idealized LV focusing on the treatment of the mitral valve. Indeed, it has been highlighted from visualizations [10, 68] that the shape and the size of the mitral valve, as well as the inlet flow profile, could severely affect the intra-ventricular vortex structures. Therefore, we perform the comparison of the intra-ventricular flow pattern either by considering different shapes (circular or elliptic) for the mitral valve or by imposing a prescribed inlet velocity profile. Our numerical study considers several fluid dynamics indicators by synthetic quantities – such as the total kinetic energy or the enstrophy – and detailed local information in space and time by accounting for e.g. the vorticity and the fluctuating kinetic energy. Our analysis shows that the blood flow in the LV is neither laminar nor fully turbulent and thus requires a suitable modelling accounting for its transitional nature; in the present work we use the Variational Multiscale Method with terms accounting for LES turbulence modeling [5].

    The outline of this work is as follows. The mathematical model for the blood flow description in an idealized LV is presented in Sec. 2. In Sec. 3, we detail its numerical approximation and the MTV BCs for the Navier-Stokes equations with their approximation by means of the ENM. In Sec. 4, we present and discuss the simulated blood flow patterns, including a comparison of the different models of the mitral valve. Conclusions follow.

2   Modeling of blood flows in an idealized left ventricle

We present the mathematical model describing the blood flow in a 3D idealized LV represented by a truncate prolate ellipsoid [2, 79, 82] which expands and contracts during the heartbeat. Such geometry, which can be exactly represented by NURBS, is described in Sec. 2.1, and with its prescribed evolution in time in Sec. 2.2. The Navier-Stokes equations in Arbitrary Lagrangian Eulerian (ALE) formulation [6, 26, 27, 28, 32, 33] are recalled in Sec. 2.3. Finally, in Sec. 2.4, we illustrate the modeling of the valves as BCs of the Navier-Stokes equations.

2.1   Left ventricle geometry and wall displacements

The idealized LV is computationally represented as a time-dependent domain $\Omega^{(t)} \subset \mathbb{R}^3$, half of a prolate ellipsoid, which is completely characterized by the lengths of its major and minor semi
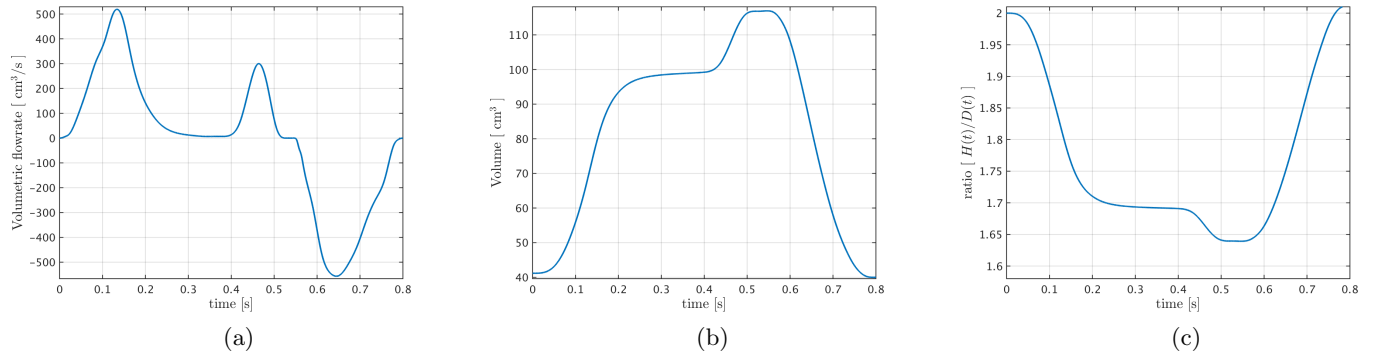
Figure 2: Prescribed volumetric flow Q vs. time [s] (a); evolution of the volume V (b) and of the ratio H/D (c) vs. time [s] along an heartbeat for the 3D idealized LV obtained by solving the system of ODEs (2.1).

axes [3, 24]. With this aim we introduce the time dependent functions $D : (0,T) \to \mathbb{R}$ and $H : (0,T) \to \mathbb{R}$, representing the height and the upper plane diameter of the ellipsoid, respectively; see Fig. 1. We assume the reference configuration $\widehat{\Omega}$ at the time instant corresponding to the beginning of the diastolic filling phase, for which the initial diameter is $D(0) \equiv D_0 = 3.4$ cm, yielding the base of the ellipsoid at the initial configuration defined, in Cartesian coordinates, as $\{(x, y, z) : x^2 + y^2 \leqslant 2.89 \text{ cm}^2, z = 0\}$. The quota $z = 0$ of the base of the ellipsoid is kept fixed, with the apex moving during the heartbeat. The height of the ellipsoid is set to $H_0 = 2D_0$, i.e. $H(0) = H_0 = 6.8$ cm. For the idealized human LV, the ratio H/D is about $1.7 \div 2$ [16, 24, 55, 82], which varies in this range during the heartbeat, as shown e.g. in Fig. 2c, according to some law prescribing the LV wall movement.

We exactly represent the 3D LV as a NURBS geometry comprised of basis functions of degree $p = 2$ starting from the geometry represented in Fig. 1b and moving the control points located on the red control polygon such that $dx = D_0/2$ and $dz = 0$. We enforce the periodicity of the basis functions through master-slave relations among the degrees of freedom (DoFs) – now located across the inner degenerated face – by suitably triggering the properties of NURBS basis functions; in fact, the NURBS basis functions are C^1-continuous in $\Omega^{(t)}$, with C^0-continuity only at the degenerate axis corresponding to the centerline of the ellipsoid.

2.2 Prescribed wall displacement of the LV

As this work focuses on the fluid dynamics of the LV rather than on the description of the LV wall behaviour or the fluid-structure interaction, following [2, 3], we prescribe a priori the LV wall displacement. Specifically, we consider a simple elastic membrane model derived from a generalized Laplace's law coupled to a given flow-discharge profile [3, 24]. By considering a simplified elastic membrane model for the LV wall and by enforcing the equality of the volumetric flow rate through the LV volume variation, i.e. $Q(t) = \dfrac{dV}{dt}(t)$ for all $t \in (0,T)$, we obtain the system of ODEs in the

unknowns $D : (0, T) \to \mathbb{R}$ and $H : (0, T) \to \mathbb{R}$ reading:

find $D(t)$ and $H(t)$:
$$
\begin{cases}
\dfrac{\mathrm{d}D}{\mathrm{d}t} = \dfrac{6Q}{\pi} \dfrac{8H^2 - D^2}{20DH^3 - 2HD^3} & \text{in } (0, T), & \text{(2.1a)} \\[2mm]
\dfrac{\mathrm{d}H}{\mathrm{d}t} = \dfrac{H}{D} \dfrac{\mathrm{d}D}{\mathrm{d}t} \dfrac{4H^2}{8H^2 - D^2} & \text{in } (0, T), & \text{(2.1b)} \\[2mm]
D(0) = D_0, & & \text{(2.1c)} \\[2mm]
H(0) = H_0. & & \text{(2.1d)}
\end{cases}
$$

where $t = 0$ corresponds to the end systolic phase, and Q is the one reported in Fig. 2a, as obtained from [3]. Here, we set the heartbeat period to $T = 0.8$ s. The flowrate profile $Q(t)$ under consideration has been adapted from clinical data; positive values of Q correspond to the diastolic phase in which the LV expands, while negative values of Q to the systolic phase in which the LV contracts. We observe that during the filling phase, the curve $Q(t)$ is characterized by two maxima corresponding to the early LV filling (E-wave) and the secondary filling, mainly associated to the atrial contraction (A-wave). From $Q(t)$ we obtain the volume evolution $V(t)$ for a healthy 3D LV represented in Fig. 2b for the initial data of the system of ODEs (2.1) $D_0 = 3.4$ cm and $H_0 = 2D_0$. We observe that the values reported in [29] for the end systolic volume (ESV $= 53 \pm 20$ cm^3) and end diastolic volume (EDV$= 137 \pm 32$ cm^3) are correctly reproduced by our model.

Once $H(t)$ and $D(t)$ are set by solving problem (2.1), (as we did by means of the explicit Runge-Kutta method [14]) we introduce the dilation functions $\lambda : (0, T) \to \mathbb{R}$ and $\mu : (0, T) \to \mathbb{R}$ given by $\lambda(t) = \dfrac{D(t)}{D_0}$ and $\mu(t) = \dfrac{H(t)}{H_0}$, respectively, which define the affine transformation governing the LV chamber dilatation. Moreover, their derivatives determine the velocity at the LV walls, say $\boldsymbol{v}^{\mathrm{W}}(\mathbf{x}, t) = \left(\dfrac{\mathrm{d}\lambda(t)}{\mathrm{d}t} \mathrm{x}, \dfrac{\mathrm{d}\lambda(t)}{\mathrm{d}t} \mathrm{y}, \dfrac{\mathrm{d}\mu(t)}{\mathrm{d}t} \mathrm{z} \right)$.

2.3   Navier-Stokes equations in ALE formulation

By assuming a Newtonian rheological behaviour for the blood, we mathematically describe the blood flow by means of the incompressible Navier-Stokes equations in ALE formulation [26, 27, 28, 32, 33] as the LV experiences large deformations along the heartbeat. We denote as $\phi^{(t)} : \widehat{\Omega} \to \Omega^{(t)}$ the ALE mapping of the reference domain $\widehat{\Omega} \subset \mathbb{R}^3$ into the current configuration $\Omega^{(t)} \subset \mathbb{R}^3$. The spatial coordinates of the current and reference configurations are here referred as $\mathbf{x}$ and $\mathbf{X}$, respectively. By denoting with $\widehat{\boldsymbol{u}}$ the domain velocity, the dimensionless Navier-Stokes equations in ALE (convective) formulation in the physical unknowns $(\boldsymbol{u}, p)$, which represent the fluid velocity and pressure in the current configuration $\Omega^{(t)}$, read:

find, for all $t \in (0, T)$, $\boldsymbol{u} : \Omega^{(t)} \to \mathbb{R}^d$ and $p : \Omega^{(t)} \to \mathbb{R}$ such that:

$$
\begin{cases}
\left. \dfrac{\partial \boldsymbol{u}}{\partial t} \right|_{\mathbf{X}} + ((\boldsymbol{u} - \widehat{\boldsymbol{u}}) \cdot \nabla) \boldsymbol{u} - \nabla \cdot \sigma(\boldsymbol{u}, p) = \boldsymbol{0} & \text{in } \Omega^{(t)}, & \text{(2.2a)} \\[3mm]
\nabla \cdot \boldsymbol{u} = 0 & \text{in } \Omega^{(t)}, & \text{(2.2b)}
\end{cases}
$$

endowed with suitable initial and BCs, where the partial time derivative is taken with respect to the (fixed) reference domain $\widehat{\Omega}$, while the partial spatial derivatives are evaluated in the current configuration; $\sigma(\boldsymbol{u}, p)$ is the Cauchy stress tensor, defined as $\sigma(\boldsymbol{u}, p) = -p\mathrm{I} + \dfrac{2}{\mathbb{R}e} D(\boldsymbol{u})$, with $\mathbb{R}e$ the Reynolds number, $D(\boldsymbol{u}) = \dfrac{(\nabla \boldsymbol{u} + \nabla \boldsymbol{u}^T)}{2}$ the strain rate tensor, and I the identity tensor. Typically,

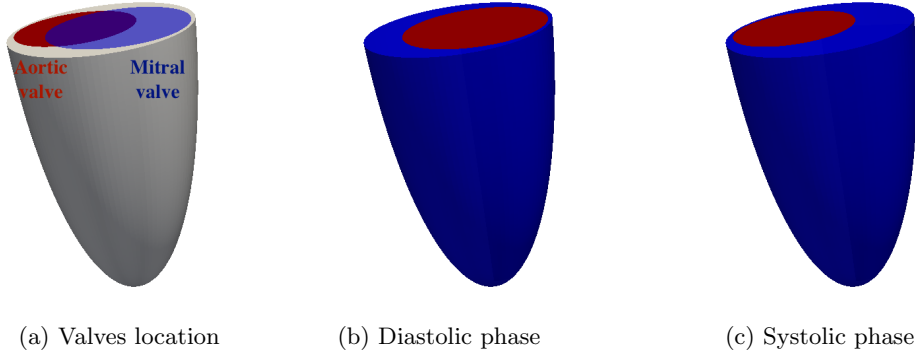(a) Valves location   (b) Diastolic phase   (c) Systolic phase

Figure 3: Mitral and aortic valves as orifices of infinitesimal thickness on the LV boundary (a); open valves as subsets of $\partial\Omega^{(t)}$ at diastole (b) and systole (c).

the initial condition of the fluid velocity is a divergence-free velocity field $\boldsymbol{u}_0 : \Omega^{(0)} \to \mathbb{R}^d$, usually $\boldsymbol{u}(\mathbf{x}, 0) = \boldsymbol{u}_0 = \boldsymbol{0}$[1]. When addressing BCs on $\partial\Omega^{(t)}$, within this work we consider the partition of the boundary $\partial\Omega^{(t)}$ in measurable subsets $\Gamma_D^{(t)}$ and $\Gamma_N^{(t)} \subseteq \partial\Omega^{(t)}$ such that $\overline{\Gamma_D^{(t)} \cup \Gamma_N^{(t)}} = \partial\Omega^{(t)}$ and $\mathring{\Gamma}_D^{(t)} \cap \mathring{\Gamma}_N^{(t)} = \varnothing$ for all $t \in (0, T)$, where we consider either Dirichlet or natural BCs [6, 7], the latter defined in terms of the total momentum flux:

$$\boldsymbol{\Phi}(\boldsymbol{u} - \hat{\boldsymbol{u}}; \boldsymbol{u}, p) = -\boldsymbol{u} \otimes (\boldsymbol{u} - \hat{\boldsymbol{u}}) + \sigma(\boldsymbol{u}, p), \qquad (2.3)$$

as we will detail in Sec. 2.4. In general, the Dirichlet and natural BCs are expressed in terms of the vector fields $\boldsymbol{g}$ and $\boldsymbol{G}$, as:

$$\boldsymbol{u} = \boldsymbol{g} \quad \text{on } \Gamma_D^{(t)}, \qquad (2.4a)$$

$$-\boldsymbol{\Phi}(\boldsymbol{u} - \hat{\boldsymbol{u}}; \boldsymbol{u}, p)\mathbf{n} = \boldsymbol{G} \quad \text{on } \Gamma_N^{(t)}, \qquad (2.4b)$$

respectively, where $\mathbf{n}$ indicates the outward directed unit vector normal to $\Gamma_N^{(t)}$.

2.4   Boundary conditions for physiological flows in the left ventricle

We prescribe physiological BCs for the Navier-Stokes equations (2.2), that are suitable to account for the valves in the idealized LV as orifices of infinitesimal thickness located on the LV equatorial plane. On the subset of the boundary $\partial\Omega^{(t)}$ corresponding to the muscle LV walls, say $\Gamma^{W,(t)}$, we impose the so-called *no-slip condition* for any $t \in (0, T)$, i.e. a Dirichlet BC which reads:

$$\boldsymbol{u} = \boldsymbol{v}^W \quad \text{on } \Gamma^{W,(t)}, \qquad (2.5)$$

where $\boldsymbol{v}^W$ denotes the velocity of the LV wall determined by solving Eq. (2.1).

The remaining subset of the boundary $\partial\Omega^{(t)}$ is constituted by the subsets $\Gamma^V = \Gamma^{AO} \cup \Gamma^{MT}$ which correspond to the aortic and mitral valves, respectively, modelled as orifices of infinitesimal thickness and located on the equatorial plane; see Fig. 3a. We highlight that, based on physiological

---

[1]For blood flows in the LV, the initial condition $\boldsymbol{u}_0 = \boldsymbol{0}$ involve non physiological initial data. Nevertheless, this effect on the solution can be considered negligible after a sufficiently long time, in this case after few heartbeats (two or three).

considerations, we assume their positions and sizes to be fixed in time, despite the LV base moves according to the wall law described in Sec. 2.2.

Accounting for the opening and closing stages of the valves through suitable BCs leads to consider different types of BCs, namely, essential and natural, switching during the heartbeat [67]. A zero velocity BC, i.e. $\boldsymbol{u} = \boldsymbol{0}$, is associated to a valve in closed configuration, while a natural BC (defective, resisistive, ...) to an open one. However, a common practice [2, 3, 23, 24, 25, 56] considers the prescription of a velocity profile on Γ^{MT}, i.e. a Dirichlet BC on Γ^{MT} representing the inlet boundary during the diastolic phase. However, this practice is too simplistic and leads to model blood flows in the LV which are not physiological; see [74]. In this section, we focus on the open phase of each valve.

2.4.1 Treatment of the open aortic valve

For modeling the open aortic valve, which is represented as the outlet LV boundary during the systole, resistance (or defective) BCs at Γ^{AO} [6, 7, 78] can be considered to ensure realistic simulations. Specifically, we prescribe at the aortic valve orifice a resistance BC of the natural type, similarly to [6, 7], i.e. the BC in Eq. (2.4b) with the prescribed stress on $\Gamma_N^{(t)}$ decomposed in its normal and tangential components as $\boldsymbol{G} = G_{\perp}\mathbf{n} + G_{\parallel}\mathbf{t}$, with $\mathbf{t}$ the unit tangent vector to $\Gamma_N^{(t)}$; we observe that at this stage $\Gamma_N^{(t)} \equiv \Gamma^{\text{AO}}$. Specifically, by setting $G_{\parallel} = 0$ and $G_{\perp} = -(C_{\text{out}}Q_{\text{out}}^{\text{AO}} + P_V)$, the tangential stresses are zero, while the normal stress is proportional to the flowrate $Q_{\text{out}}^{\text{AO}}$ on the boundary Γ^{AO} through the coefficient C_{out} up to the constant P_V. The former (C_{out}) represents a *resistance constant*, whose values can be obtained by *in vivo* measurements [69] (its dimensional units are dyn·s/cm^5), while P_V sets a physiologically realistic pressure

We anticipate that numerical instabilities may arise with natural BCs on Γ^{AO} in the presence of backflow reversal [60], an aspect which is crucial in blood flow simulations and requires a careful treatment. Several methods have been proposed for the treatment of outlets to preserve numerical stability [12, 60]. We will address this issue with the ENM formulation in Sec. 3.

2.4.2 Treatment of the open mitral valve

The mitral valve can be referred as the inlet boundary through which the LV is filled during diastole. Two different filling phases can be distinguished during diastole: a first rapid filling phase, called E-wave, characterized by high flowrate values, and a second one, called A-wave, caused by the atria contraction; the two maxima of the volumetric discharge $Q(t)$ in Fig. 2a correspond to the E- and A-waves, respectively. There is a strong dependence of the intraventricular fluid dynamics on the inflow velocity [2], and specifically, on the intensity of the E- and A-waves, as well as the size and shape of the mitral valve orifice.

The general lack of accurate clinical data describing the inflow velocity profile through the mitral valve in a quantitative manner prevents the use of Dirichlet BCs for the open valve phase; indeed, the velocity field at Γ^{MT} should be considered as an unknown of the LV blood flow problem. The use of a natural boundary condition for the open configuration in place of an imposed inlet profile, removes the need to make such choice a priori. Specifically, we will consider a resistance BCs of the natural type similarly to that imposed at the outlet. Nevertheless, such natural BC may still lead to unrealistic velocity profiles at the mitral valve because the standard resistance BC is too simplistic to account for an inflow associated to a moving domain. In order to prevent unrealistic inflow profiles, we propose a regularization term to be added to the standard resistance BC. This

weakly penalizes the inflow velocity profiles which are too dissimilar from the parabolic one and it is based on the second-order Laplace-Beltrami operator; in this manner, the BC of Eq. (2.4b) reads:

$$- \boldsymbol{\Phi}(\boldsymbol{u} - \widehat{\boldsymbol{u}}; \boldsymbol{u}, p)\mathbf{n} - \widetilde{\alpha^{\mathrm{MT}}} \triangle_\Gamma u = \boldsymbol{G}(\mathbf{x}, t) \quad \text{on } \Gamma_N^{(t)}, \tag{2.6}$$

where $\widetilde{\alpha^{\mathrm{MT}}}$ is a positive real parameter and the prescribed stress $\boldsymbol{G}$ is set as in Sec. 2.4.1; in this case we have $\Gamma_N^{(t)} \equiv \Gamma^{\mathrm{MT}}$.

To investigate the dependence of the intraventricular fluid dynamics on the inlet condition, we will also consider a more standard approach where an inflow velocity profile is prescribed at the valve through Dirichlet BCs. Specifically, we impose a pulsatile periodic inlet flow profile compatible with the flowrate $Q(t)$ of Fig. 2a by considering a parabolic-type profile at Γ^{MT}. We assume a circular shape for the mitral valve denoting with $\boldsymbol{\epsilon}_{\mathrm{MT}}$ the eccentric position of the mitral orifice with respect to the vertical axis of the LV and with r_{MT} the radius of the mitral orifice, respectively. Then, we characterize the function $\boldsymbol{g}^{\mathrm{MT}}$ defining the Dirichlet BC in Eq. (2.4a) for Γ^{MT} as:

$$\boldsymbol{g}^{\mathrm{MT}} : \Gamma^{\mathrm{MT}} \times (0, T) \to \mathbb{R}^d \quad : \quad \boldsymbol{g}^{\mathrm{MT}}(\mathbf{x}, t) = \boldsymbol{v}^{\mathrm{MT}}(\mathbf{x})q(t), \tag{2.7}$$

with $\boldsymbol{v}^{\mathrm{MT}} : \Gamma^{\mathrm{MT}} \to \mathbb{R}^d$ and $q : (0, T) \to \mathbb{R}$ a vector and a scalar valued functions, respectively. Specifically, by considering dimensionless quantities for $\boldsymbol{\epsilon}_{\mathrm{MT}}$ and r_{MT}, we define $\boldsymbol{v}^{\mathrm{MT}} = \left(\boldsymbol{v}_{\mathrm{x}}^{\mathrm{W}}, \boldsymbol{v}_{\mathrm{y}}^{\mathrm{W}}, a_{\mathrm{P}} \|\mathbf{x} - \boldsymbol{\epsilon}_{\mathrm{MT}}\|_2^2 - b_{\mathrm{P}} \right)$ where a_{P} and b_{P} define the paraboloid with unitary volume passing through the valve boundary. Moreover, $q(t) = Q^{\mathrm{MT}}(t)\chi_{\{Q^{\mathrm{MT}}(t)>0\}}$ is defined in terms of the dimensionless counterpart of the inlet flowrate $Q^{\mathrm{MT}}(t) = Q(t) - Q^{\mathrm{W}}(t)$, which can be exactly computed at each time instant by the evaluation of $Q(t)$ (Fig. 2a) and the analytical expression of $Q^{\mathrm{W}}(t) = \int_{\Gamma^{\mathrm{W},(t)}} \boldsymbol{v}^{\mathrm{W}} \cdot \mathbf{n} \, \mathrm{d}\Gamma$ obtained by using $D(t)$, $H(t)$, $\dfrac{\mathrm{d}D(t)}{\mathrm{d}t}$, and $\dfrac{\mathrm{d}H(t)}{\mathrm{d}t}$.

3   Numerical approximation of the Navier-Stokes equations

We approximate the Navier-Stokes equations (2.2) complemented with the BCs of Sec. 2.4 by considering NURBS-based IGA in the framework of the Galerkin method [4, 6, 19, 21] for the spatial approximation, and the generalized-α method [17, 43, 81] for the time discretization. However, accounting for the valves functioning through BCs switching in time from essential to natural and viceversa, is far from being a trivial task from both the mathematical and numerical points of view. Indeed, the Dirichlet and natural subsets of the boundary $\partial\Omega^{(t)}$ vary during an heartbeat and correspond to $\Gamma_D^{(t)} = \Gamma^{\mathrm{AO}} \cup \Gamma^{\mathrm{W},(t)}$ and $\Gamma_N^{(t)} = \Gamma^{\mathrm{MT}}$, respectively, in the diastolic phase; while, during the systolic phase, to $\Gamma_D^{(t)} = \Gamma^{\mathrm{MT}} \cup \Gamma^{\mathrm{W},(t)}$ and $\Gamma_N^{(t)} = \Gamma^{\mathrm{AO}}$, respectively (see Fig. 3). A standard (strong) imposition of Dirichlet BCs leads to consider a family of closed time-varying function subspaces depending on $\Gamma_D^{(t)}$. Moreover, from the discrete point of view, both the size and the structure of the associated discrete problem change and all these drawbacks could considerably affect the computational performances. In order to circumvent these difficulties, we use the Extended Nitsche's method (ENM) for mixed time-varying (MTV) BCs for the Navier-Stokes equations [76] which prevents the use of time varying function spaces. Moreover, the formulation additionally features the occurrence of the numerical instabilities due to the partial or total flow reversal associated to resistance BCs of Sec. 2.4.1.

Finally, we consider the Variational Multiscale Method (VMS) for the Navier-Stokes equations with terms accounting for Large Eddy Simulation (LES) modeling of [5] to obtain a stabilized

Galerkin formulation of the Navier-Stokes equations satisfying the Babuška-Brezzi condition [13, 65] The use of the VMS-LES formulation allows also to control the numerical instabilities due to the advective regime occurring at high Reynolds numbers and to numerically model turbulence according to the LES paradigm.

3.1   Spatial approximation by IGA

In order to perform the spatial discretization by means of NURBS-based IGA, we firstly represent the reference domain $\widehat{\Omega}$ as a NURBS geometry as described in Sec. 2.1. Specifically, let $\{\widehat{\mathbf{P}}_A\}_{A=1}^{N_b}$ and $\{\widehat{\boldsymbol{N}}_A\}_{A=1}^{N_b}$ be the control points and the set of NURBS basis functions defining the NURBS geometry through the mapping $\mathbf{X} = \sum_{A=1}^{N_b} \widehat{\mathbf{P}}_A \widehat{N}_A(\mathbf{X})$ and the associated NURBS space $\widehat{\mathcal{N}}_h = \operatorname{span}\left\{\widehat{\boldsymbol{N}}_A\right\}_{A=1}^{N_b}$. In virtue of the affine covariance property holding for NURBS geometries, the discrete ALE mapping is defined as:

$$\phi^{(t)}(X) = \sum_{A=1}^{N_b} (\widehat{\mathbf{P}}_A + \mathbf{d}_A(t))\widehat{\boldsymbol{N}}_A(\mathbf{X}) \tag{3.1}$$

where $\{\mathbf{d}_A(t)\}_{A=1}^{N_b}$ represents the set of the displacement vectors of the control points following the prescribed LV deformation. Consequently, the fluid domain motion and the representation of the current configuration $\Omega^{(t)}$ are controlled by the displacement of these NURBS control points. Moreover, we define the space of NURBS in $\Omega^{(t)}$ as the push-forward of the space $\widehat{\mathcal{N}}_h = \operatorname{span}\{\widehat{\boldsymbol{N}}_A\}_{A=1}^{N_b}$, i.e. $\mathcal{N}_h^{(t)} = \operatorname{span}\{\widehat{\boldsymbol{N}}_A \circ \phi^{(t)^{-1}}\}_{A=1}^{N_b} = \operatorname{span}\{\boldsymbol{N}_A^{(t)}\}_{A=1}^{N_b}$. The NURBS mesh associated to $\Omega^{(t)}$ is denoted by $\mathcal{T}_h^{(t)}$, with $h_T^{(t)} = \operatorname{diam} T^{(t)}$ the diameter of a general element $T^{(t)} \in \mathcal{T}_h^{(t)}$ and $h^{(t)} = \max_{T^{(t)} \in \mathcal{T}_h^{(t)}} h_T^{(t)}$ the characteristic mesh size. Moreover, let the boundary $\Gamma^{(t)}$ be split into N_{eb} subsets corresponding to the edges of the elements $T_b \subseteq \mathcal{T}_h^{(t)}$ such that $\partial T_b \cap \Gamma^{\mathrm{V}} \neq \varnothing$, for $b = 1, \ldots, N_{eb}$. We define $\Gamma_b = \partial T_b \cap \Gamma^{\mathrm{V}}$ and we introduce the size h_b of Γ_b, for $b = 1, \ldots, N_{eb}$, by using the covariant element metric tensor $\mathbf{G}$ as $h_b = 2(\boldsymbol{t}^T \mathbf{G} \boldsymbol{t})^{-1/2}$, where $\boldsymbol{t}$ is the unit vector tangent to the boundary element ∂T_b.

3.2   Semi-discrete formulation

The equations (2.2) are formulated in terms of the unknowns $(\boldsymbol{u}, p)$ in the current configuration expressed as a function of $\mathbf{x} \in \Omega^{(t)}$, for all $t \in (0, T)$. When considering NURBS-based IGA in the framework of the Galerkin method, we look for an approximate solution as an element of the NURBS space $\mathcal{N}_h^{(t)}$, i.e. $\boldsymbol{u}_h(\mathbf{x}, t) = \sum_{A=1}^{N_b} \boldsymbol{u}_A(t) \boldsymbol{N}_A^{(t)}(\mathbf{x})$ and $p_h(\mathbf{x}, t) = \sum_{A=1}^{N_b} p_A(t) \boldsymbol{N}_A^{(t)}(\mathbf{x})$, where $\{\boldsymbol{u}_A(t)\}_{A=1}^{N_b}$ and $\{p_A(t)\}_{A=1}^{N_b}$ are the control variables associated to the velocity and the pressure at $t \in (0, T)$, respectively. Moreover, since the fluid domain deformation can be expressed in terms of $\boldsymbol{N}_A^{(t)}(\mathbf{x})$, the fluid domain velocity in the current configuration is defined as $\widehat{\boldsymbol{u}}_h(\mathbf{x}, t) = \sum_{A=1}^{N_b} \dot{\mathbf{d}}_A(t) \boldsymbol{N}_A^{(t)}(\mathbf{x})$.

By strongly enforcing a non-slip condition for any $t \in (0, T)$ on $\Gamma^{\mathrm{W},(t)}$, we define the finite dimensional test and trial function spaces for the velocity $\mathcal{V}_h^{(t)}$ and $\mathcal{W}_h^{(t)}$ as $\mathcal{V}_h^{(t)} = \mathcal{V}^{(t)} \cap \left[\mathcal{N}_h^{(t)}\right]^3$

and $\mathcal{W}_h^{(t)} = \mathcal{W}^{(t)} \cap \left[\mathcal{N}_h^{(t)} \right]^3$, respectively, where:

$$\mathcal{V}^{(t)} = \{ \boldsymbol{u} \in [\mathrm{H}^1(\Omega^{(t)})]^3 : \boldsymbol{u} = \boldsymbol{v}^{\mathrm{W}} \text{ on } \Gamma^{\mathrm{W},(t)} \} \text{ and } \mathcal{W}^{(t)} = \{ \boldsymbol{u} \in [\mathrm{H}^1(\Omega^{(t)})]^3 : \boldsymbol{u} = \boldsymbol{0} \text{ on } \Gamma^{\mathrm{W},(t)} \}, \quad (3.2)$$

for $t \in (0, T)$; while, for the pressure $\mathcal{Q}_h^{(t)} = \mathcal{Q}^{(t)} \cap \mathcal{N}_h^{(t)}$, with $\mathcal{Q}^{(t)} = \mathrm{L}^2(\Omega^{(t)})$.

The semi-discrete form of the weak formulation of the Navier-Stokes equations (2.2) with the weak imposition of the MTV BCs of Sec. 2.4 by means of the ENM reads:

find, for all $t \in (0, T)$, $(\boldsymbol{u}_h, p_h) \in \mathcal{V}_h^{(t)} \times \mathcal{Q}_h^{(t)}$ such that:

$$\mathcal{B}((\boldsymbol{\varphi}_h, q_h), (\boldsymbol{u}_h, p_h); \widehat{\boldsymbol{u}}_h) - \mathcal{F}(\boldsymbol{\varphi}_h, q_h) + \mathcal{I}((\boldsymbol{\varphi}_h, q_h), (\boldsymbol{u}_h, p_h); \widehat{\boldsymbol{u}}_h) = 0, \quad \forall (\boldsymbol{\varphi}_h, q_h) \in \mathcal{W}_h^{(t)} \times \mathcal{Q}_h^{(t)}, \quad (3.3)$$

where:

$$\mathcal{B}((\boldsymbol{\varphi}, q), (\boldsymbol{u}, p); \widehat{\boldsymbol{u}}) = \int_{\Omega^{(t)}} \boldsymbol{\varphi} \cdot \frac{\partial \boldsymbol{u}}{\partial t} \, \mathrm{d}\Omega + \frac{2}{\mathbb{R}e} \int_{\Omega^{(t)}} D(\boldsymbol{\varphi}) : D(\boldsymbol{u}) \, \mathrm{d}\Omega + \int_{\Omega^{(t)}} \boldsymbol{\varphi} \cdot ((\boldsymbol{u} - \widehat{\boldsymbol{u}}) \cdot \nabla) \, \boldsymbol{u} \, \mathrm{d}\Omega$$

$$- \int_{\Omega^{(t)}} p \, \nabla \cdot \boldsymbol{\varphi} \, \mathrm{d}\Omega + \int_{\Omega^{(t)}} q \, \nabla \cdot \boldsymbol{u} \, \mathrm{d}\Omega, \qquad (3.4\mathrm{a})$$

$$\mathcal{F}(\boldsymbol{\varphi}, q) = \int_{\Omega^{(t)}} \boldsymbol{\varphi} \cdot \boldsymbol{f} \, \mathrm{d}\Omega. \qquad (3.4\mathrm{b})$$

Moreover, the term $\mathcal{I}$, accounting for the BCs of Sec. 2.4 imposed through the ENM for MTV BCs, reads:

$$\begin{aligned}
\mathcal{I}_h((\boldsymbol{\varphi}, q), (\boldsymbol{u}, p), \widehat{\boldsymbol{u}}) = \sum_{b=1}^{N_{eb}} &\left[\int_{\Gamma_b} \left(-\frac{\gamma h_b}{\xi + \gamma h_b} \right) \boldsymbol{\varphi} \cdot (\boldsymbol{\Phi}(\boldsymbol{u} - \widehat{\boldsymbol{u}}; \boldsymbol{u}, p)\mathbf{n}) \, \mathrm{d}\Gamma \right. \\
&+ \int_{\Gamma_b} \left(-\frac{\gamma h_b}{\xi + \gamma h_b} \right) (\boldsymbol{\Phi}_{in}^*(\boldsymbol{u} - \widehat{\boldsymbol{u}}; \boldsymbol{\varphi})\mathbf{n}) \cdot (\boldsymbol{u} - \boldsymbol{g}) \, \mathrm{d}\Gamma \\
&+ \int_{\Gamma_b} \left(\frac{\xi \gamma}{\mathbb{R}e(\xi + \gamma h_b)} \right) \boldsymbol{\varphi} \cdot (\boldsymbol{u} - \boldsymbol{g}) \, \mathrm{d}\Gamma \\
&+ \int_{\Gamma_b} \left(-\frac{\mathbb{R}e \, h_b}{\xi + \gamma h_b} \right) \boldsymbol{\Phi}_{in}^*(\boldsymbol{u} - \widehat{\boldsymbol{u}}; \boldsymbol{\varphi})\mathbf{n} \cdot (\boldsymbol{\Phi}(\boldsymbol{u} - \widehat{\boldsymbol{u}}; \boldsymbol{u}, p)\mathbf{n} - \boldsymbol{G}) \, \mathrm{d}\Gamma \\
&- \left. \int_{\Gamma_b} \left(\frac{\xi}{\xi + \gamma h_b} \right) \boldsymbol{\varphi} \cdot \boldsymbol{G} \, \mathrm{d}\Gamma \right] \\
&+ \sum_{b=1}^{N_{eb}} \left[- \int_{\Gamma_b} \alpha^{\mathrm{MT}} \left(D(\boldsymbol{u}) : D(\boldsymbol{\varphi}) \right) \, \mathrm{d}\Gamma \right],
\end{aligned} \qquad (3.5)$$

where $\boldsymbol{G}$ is the function defining the resistance BC described in Sec. 2.4.1 used for the open valve, and $\boldsymbol{g}$ defines the no-slip BC mimicking the closed valve (ideally, in a fixed ventricle, we have $\boldsymbol{g} = \boldsymbol{0}$). $\boldsymbol{\Phi}_{in}^*$ is the *adjoint inflow total flux*, which, within the ALE formulation, reads $\boldsymbol{\Phi}_{in}^*(\boldsymbol{u} - \widehat{\boldsymbol{u}}; \boldsymbol{\varphi}) = (\boldsymbol{\varphi} \otimes (\boldsymbol{u} - \widehat{\boldsymbol{u}}))\chi_{\{(\boldsymbol{u}-\widehat{\boldsymbol{u}})\cdot\mathbf{n}<0\}} + \frac{2}{\mathbb{R}e}D(\boldsymbol{\varphi})$, for which $\boldsymbol{\Phi}_{in}^*(\boldsymbol{u} - \widehat{\boldsymbol{u}}; \boldsymbol{\varphi})\mathbf{n} = \{(\boldsymbol{u} - \widehat{\boldsymbol{u}}) \cdot \mathbf{n}\}_- \cdot \boldsymbol{\varphi} + \frac{2}{\mathbb{R}e}D(\boldsymbol{\varphi})\mathbf{n}$, where $\{(\boldsymbol{u} - \widehat{\boldsymbol{u}}) \cdot \mathbf{n}\}_- = \dfrac{(\boldsymbol{u} - \widehat{\boldsymbol{u}}) \cdot \mathbf{n} - |(\boldsymbol{u} - \widehat{\boldsymbol{u}}) \cdot \mathbf{n}|}{2}$. The adjoint inflow total flux $\boldsymbol{\Phi}_{in}^*$ has been introduced in analogy with the weak enforcement of the Dirichlet BC for the advection-diffusion equation of [8] to handle ad hoc the BCs at the inlet and outlet subsets of the boundary. Indeed, if Γ_b lays on an outlet boundary (for which $\boldsymbol{u} \cdot \mathbf{n} > 0$), only the diffusive part of the total flux

operator $\boldsymbol{\Phi}$ is considered for the weighting function $\boldsymbol{\varphi}$, while, if Γ_b lays on an inlet boundary, we take into account both the diffusive and advective parts for the weighting function $\boldsymbol{\varphi}$.

The last term in Eq. (3.5) is due to the flow regularization introduced in Eq. (2.6) and switches on only in correspondence of the mitral valve orifice in its open configuration by definition of the function $\alpha^{\mathrm{MT}} : \Gamma^{\mathrm{V}} \times (0, T) \to (0, +\infty)$ as $\alpha^{\mathrm{MT}}(\mathbf{x}, t) = \widetilde{\alpha^{\mathrm{MT}}} \; \chi_{\{\mathbf{x} \in \Gamma^{\mathrm{MT}}\}} \; \chi_{\{Q(t) > 0\}}$.

The remaining boundary terms are associated to the weak imposition of the MTV BCs by means of the ENM and allow the simulation of the opening and closing phases of the valves by a suitable tuning of the function $\gamma : \Gamma^{\mathrm{V}} \times (0, T) \to (0, +\infty)$. Specifically, we observe that by taking the limit $\gamma \to \infty$ in Eq. (3.5), we recover the original weak imposition of the Dirichlet BCs for the Navier-Stokes equations (2.2) presented in [8] in the ALE case. As a matter of fact, the weak imposition of Dirichlet BCs of [8] represents a particular case of the more general scheme that we initially proposed in [76]. Precisely, for $\gamma \to \infty$, only the first three boundary terms of Eq. (3.5) play a role and are associated to the weak imposition of the essential BCs. The first one is the so called consistency term, while the other two are responsible for the weak enforcement of the Dirichlet data $\boldsymbol{g}$, with the last term being penalty-like through the function ξ (its weight is $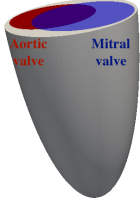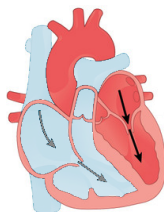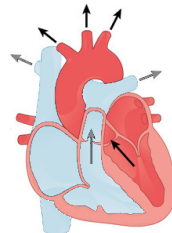\dfrac{\xi^{\mathrm{AO}}}{\mathbb{R}e \; h_b}$). Similarly to [8], in such boundary term the dependency on h_b^{-1} allows to recover the optimal rate of convergence, while the scaling with respect to $\mathbb{R}e$ yields dimensional consistency and automatically regulates the contribution of this boundary term depending on the flow regime. Still for $\gamma \to \infty$, the last two boundary terms in Eq. (3.5) vanish. Contrarily, in the limit $\gamma \to 0$ in Eq. (3.5), we are weakly imposing natural type BCs. In this case, only the third and the fourth boundary terms of Eq. (3.5) are active. The first, a penalty-like term weighted by $\dfrac{\mathbb{R}e \; h_b}{\xi^{\mathrm{AO}}}$ (for $\gamma \to 0$) is in addition to the standard term obtained in the weak formulation of the problem with natural BCs and assumes a stabilization role in preventing the occurrence of the numerical instabilities caused by the partial or total flow reversal through an outlet boundary. This boundary term can be compared to the artificial traction term proposed in [7] and further developed in [60] to prevent backflow divergence at outlet boundary. Finally, the fourth term in Eq. (3.5), corresponds to the standard weak imposition of natural BCs.

Concerning the function $\xi : \Gamma^{\mathrm{V}} \times (0, T) \to (0, +\infty)$ this is a positive, bounded, and time dependent real-valued function acting as a penalty function. Specifically, we observe that for $\gamma \to \infty$ (i.e. for the weak imposition of the essential BCs on Γ^{V}) the larger is the value of ξ, the stronger is the penalization associated to such BCs. Conversely, for $\gamma \to 0$ (for the natural type BCs on Γ^{AO}) the smaller is the value of ξ, the larger is the contribution of the stabilization term preventing backflow divergence. Therefore, similarly to γ, we also consider ξ as a space-time dependent real positive function $\xi : \Gamma^{\mathrm{V}} \times (0, T) \to \mathbb{R}$. Specifically, we suppose ξ to be a measurable bounded function for which there exist two positive constants such that $0 < \overline{\xi}_0 < \xi(\mathbf{x}, t) < +\infty$ and $0 < \xi(\mathbf{x}, t) < \overline{\xi}_\infty < +\infty$ for all $(\mathbf{x}, t) \in \bigcup\limits_{b=1}^{N_{eb}} \Gamma_b \times (0, T)$. Such constants, $\overline{\xi}_0$ and $\overline{\xi}_\infty$, depend on the problem data (i.e. the Reynolds number $\mathbb{R}e$ and the shape of the domain), on local boundary inverse estimates, and on the order of interpolation used in the finite dimensional space; see [8, 18]. $\overline{\xi}_0$ and $\overline{\xi}_\infty$ can be estimated by extending the analysis of [75] performed for the simpler case of parabolic PDEs complemented with MTV BCs to the Oseen problem. Generally speaking, $\overline{\xi}_0$ should be taken as "sufficiently small" and $\overline{\xi}_\infty$ "large".

A guideline for choosing γ and ξ for the mitral and aortic valves at the diastolic and systolic phases of the heartbeat is sketched in Tab. 1.

Table 1: Sketch of the choice of the functions γ and ξ at diastole and systole to represent the aortic and mitral valves through MTV BCs and the ENM.

Valve	Diastole	Systole
Aortic	**closed**	**open**
	$\gamma \to +\infty \quad \xi \to \overline{\xi}_\infty$	$\gamma \to 0 \quad \xi \to \overline{\xi}_0$
Mitral	**open**	**closed**
	$\gamma \to 0 \quad \xi \to \overline{\xi}_0$	$\gamma \to +\infty \quad \xi \to \overline{\xi}_\infty$

3.3   VMS-LES modeling of the Navier-Stokes equations in ALE formulation

For velocity and pressure discretization spaces based on polynomials or NURBS of the same degree p, the Babuška-Brezzi condition [13, 65] is not satisfied and we need to consider a stabilized Galerkin formulation of the Navier-Stokes equations. Several stabilized methods have been proposed in the literature, see e.g. [13]. However, in this work, we refer to the VMS-LES method [5, 6, 19, 20, 21, 34, 77], since it yields a stable formulation, it controls numerical instabilities due to transport dominated regime, and it provides LES modeling of turbulence. The semi-discrete formulation of problem (3.3) with VMS-LES reads:

find, for all $t \in (0, T)$, $(\boldsymbol{u}_h, p_h) \in \mathcal{V}_h^{(t)} \times \mathcal{Q}_h^{(t)}$ such that:

$$\mathcal{R}^{\mathrm{VMS}}((\boldsymbol{\varphi}_h, q_h), (\boldsymbol{u}_h, p_h); \widehat{\boldsymbol{u}}_h) = 0 \quad \forall(\boldsymbol{\varphi}_h, q_h) \in \mathcal{W}_h^{(t)} \times \mathcal{Q}_h^{(t)}, \tag{3.6}$$

where $\mathcal{R}^{\mathrm{VMS}}((\boldsymbol{\varphi}_h, q_h), (\boldsymbol{u}_h, p_h); \widehat{\boldsymbol{u}}_h)$ is defined as:

$$\mathcal{R}^{\mathrm{VMS}}((\boldsymbol{\varphi}_h, q_h), (\boldsymbol{u}_h, p_h); \widehat{\boldsymbol{u}}_h) = \mathcal{B}((\boldsymbol{\varphi}_h, q_h), (\boldsymbol{u}_h, p_h); \widehat{\boldsymbol{u}}_h) - \mathcal{F}(\boldsymbol{\varphi}_h, q_h) \tag{3.7}$$

$$+ \mathcal{I}((\boldsymbol{\varphi}_h, q_h), (\boldsymbol{u}_h, p_h); \widehat{\boldsymbol{u}}_h) \tag{3.8}$$

$$+ \sum_{T \in \mathcal{T}_h} \big[\, ((\boldsymbol{u}_h - \widehat{\boldsymbol{u}}_h) \cdot \nabla \boldsymbol{\varphi}_h, \tau_M Res_M(\boldsymbol{u}_h, p_h))_{\mathrm{L}^2(T)} + (\nabla \cdot \boldsymbol{\varphi}_h, \tau_C Res_C(\boldsymbol{s}_h))_{\mathrm{L}^2(T)}$$

$$+ \big((\boldsymbol{u}_h - \widehat{\boldsymbol{u}}_h) \cdot \nabla \boldsymbol{\varphi}_h^T, \tau_M Res_M(\boldsymbol{u}_h, p_h)\big)_{\mathrm{L}^2(T)} + (\nabla q_h, \tau_M Res_M(\boldsymbol{u}_h, p_h))_{\mathrm{L}^2(T)}$$

$$- (\nabla \boldsymbol{\varphi}_h, \tau_M Res_M(\boldsymbol{u}_h, p_h) \otimes \tau_M Res_M(\boldsymbol{u}_h, p_h))_{\mathrm{L}^2(T)} \big],$$

with $\mathcal{B}((\boldsymbol{\varphi}_h, q_h), (\boldsymbol{u}_h, p_h); \widehat{\boldsymbol{u}}_h)$ and $\mathcal{F}(\boldsymbol{\varphi}_h, q_h)$ defined in Eq. (3.4); the strong residuals of the momentum and mass equations $Res_M(\boldsymbol{u}_h, p_h)$ and $Res_C(\boldsymbol{u}_h, p_h)$ and the stabilization parameters

τ_M and τ_C are given by:

$$Res_M(\boldsymbol{u}_h, p_h) = \frac{\partial \boldsymbol{u}_h}{\partial t} + ((\boldsymbol{u}_h - \widehat{\boldsymbol{u}}_h) \cdot \nabla)\boldsymbol{u}_h + \nabla p_h - \frac{2}{\mathbb{R}e}\nabla \cdot (D(\boldsymbol{u}_h)) - \boldsymbol{f}, \tag{3.9a}$$

$$Res_C(\boldsymbol{u}_h, p_h) = \nabla \cdot \boldsymbol{u}_h, \tag{3.9b}$$

$$\tau_M = \left[\frac{4}{\Delta t^2} + (\boldsymbol{u}_h - \widehat{\boldsymbol{u}}_h) \cdot \boldsymbol{\mathcal{G}}(\boldsymbol{u}_h - \widehat{\boldsymbol{u}}_h) + C_I \frac{1}{\mathbb{R}e^2}\boldsymbol{\mathcal{G}} : \boldsymbol{\mathcal{G}}\right]^{-\frac{1}{2}}, \tag{3.9c}$$

$$\tau_C = \frac{1}{\tau_M \boldsymbol{\iota} \cdot \boldsymbol{\iota}}, \tag{3.9d}$$

$\boldsymbol{\mathcal{G}}$ being the covariant metric tensor related to the geometrical mapping from the physical to the parametric coordinates $\boldsymbol{\eta} = (\eta_1, \ldots, \eta_d)$ defined component-wise as $\mathcal{G}_{i,j} = \sum_{k=1}^{d} \frac{\partial \eta_k}{\partial \mathrm{x}_i}\frac{\partial \eta_k}{\partial \mathrm{x}_j}$ for $i, j = 1, \ldots, d$, and $\iota_i = \sum_{k=1}^{d} \frac{\partial \eta_k}{\partial \mathrm{x}_i}$, for $i = 1, \ldots, d$. The constant $C_I > 0$ is independent of the mesh size, but depends on the degree p of the NURBS basis functions, which, following an element-wise inverse estimate, we set as $C_I = 60 \cdot 2^{p-2}$ [81]; even if we have not formally introduced the time discretization yet, Δt stands for the time step size.

In order to perform the time discretization of the semi-discrete scheme of Eq. (3.6), we use the generalized-α method [43, 81] coupled to a predictor-multicorrector algorithm at each time step, we refer the reader to e.g. [22].

4 Numerical results: blood flow in the idealized left ventricle

In this section, we present the numerical study of the blood flow dynamics in an healthy idealized 3D LV with the prescribed wall motion described in Secs. 2.1–2.2. Specifically, in Sec. 4.1, we consider the treatment of both the valves through MTV BCs, thus assessing the formulation of Sec. 3, and we analyse the 3D blood flow inside the LV. Then, we analyse the dependence of the intraventricular flow on both the inflow velocity profile (Sec. 4.2) at the mitral valve and the shape of the mitral valve orifice (Sec. 4.3). A detailed analysis of the flow is performed by considering both instantaneous and phase-averaged quantities of interest as in [16].

We consider the time dependent domain $\Omega^{(t)}$ of Fig. 1 described in Sec. 2, with equatorial diameter $D(t)$ and height $H(t)$ being solutions of the systems of ODEs (2.1) with initial conditions $D(0) = D_0 = 3.4$ cm and $H(0) = H_0 = 2D_0$, yielding $D = 5.5$ cm and $H/D = 1.58$ at the end of the diastolic phase, the latter being the mean values of human LV in healthy subjects [3, 54]. The domain $\Omega^{(t)}$ is exactly represented by means of globally C^1-continuous a.e. NURBS basis functions of degree $p = 2$ and for the NURBS space $\mathcal{N}_h$ we use a mesh comprised of $N_{\mathrm{el}} = 111,622$ elements, for a total of 524,400 DoFs for the velocity and pressure variables.

The heartbeat period is set as $T_{\mathrm{HB}} = 0.8$ s and, following [73], we define the time step by referring to the characteristic mesh size and velocity, corresponding to a dimensional time step $\Delta t = 8.65 \cdot 10^{-4}$ s. The initial condition of the fluid velocity reads $\boldsymbol{u}(\mathbf{x}, 0) = \boldsymbol{u}_0 = \mathbf{0}$ in $\Omega^{(0)}$. The blood is considered as a Newtonian fluid, with constant density $\rho = 1.06$ g/cm^3 and dynamic viscosity $\mu = 4 \cdot 10^{-2}$ g/(cm $\cdot$ s). Moreover, the constant for the resistance BCs of Sec. 2.4.1 is $C_{\mathrm{out}} = 0$.
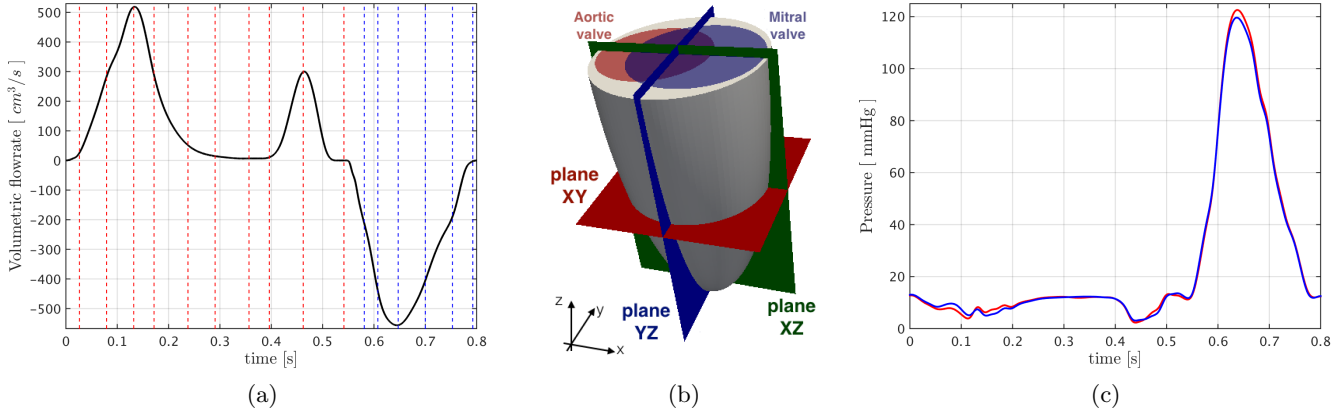
Figure 4: (a) Time instances at which the numerical results are visualized in Figs. 5-**??** during the heartbeat for the diastolic (−) and systolic (−) phases. (b) Idealized 3D LV with planes used for the visualization of Figs. 6-7: plane XZ passing throught the origin (blue), plane YZ passing throught the origin (green), and plane XY through the point $(0, \ 0, \ -3)^T$ cm (red). (c) Evolution of the phase-averaged pressure field at points in the LV near the aortic (−) and mitral (−) valves.

The numerical simulations have been performed in parallel with 80 cores on *Deneb* Cluster of EPFL; the linear solver used was GMRES with a two-level additive Schwarz preconditioner provided by *Ifpack* with *Umfpack* coarse solver. For the numerical study, we simulate up to ten heartbeats and we disregard initial three beats to remove non-physiological solutions from the analysis (in total $16'354$ time steps are simulated for our analysis).

The orifices of infinitesimal thickness representing the mitral and aortic valves and identifying the inlet and outlet subsets of the boundary are located on the upper part of the LV as shown in Fig. 3a. Specifically, unless otherwise specified, the dimensional eccentric position of the mitral valve with respect to the vertical axis of the LV is $\boldsymbol{\epsilon}_{\mathrm{MT}} = (0.35, \ 0, \ 0)^T$ cm and the radius of the mitral orifice is $r_{\mathrm{MT}} = 1.38$ cm; the ones related to the aortic valve are $\boldsymbol{\epsilon}_{\mathrm{AO}} = (-0.53, \ 0, \ 0)^T$ cm and $r_{\mathrm{AO}} = 1.19$ cm, respectively. The latter values has been chosen by assuming a circular shape for both the valves with positions and sizes kept fixed in time independently of the LV base dilation and contraction; in particular, we refer to orifices with area equal to $A_{\mathrm{MT}} = 5.98$ cm^2 and $A_{\mathrm{AO}} = 4.45$ cm^2 for the mitral and aortic valves, respectively, according to physiological values reported by the University of Nebraska Medical Center.

4.1 Blood flow in the LV

We simulate the intraventricular blood flow patterns by solving the Navier-Stokes equations endowed with the MTV BCs for the treatment of both the aortic and mitral valves of Sec. 3. Specifically, by referring to Eq. (3.5), we set $\gamma(\mathbf{x}, t) = 10^{10} \left(\chi_{\{Q(t)>0\}} \chi_{\{\mathbf{x} \in \Gamma^{\mathrm{AO}}\}} + \chi_{\{Q(t)<0\}} \chi_{\{\mathbf{x} \in \Gamma^{\mathrm{MT}}\}} \right)$
$+10^{-7} \left(\chi_{\{Q(t)>0\}} \chi_{\{\mathbf{x} \in \Gamma^{\mathrm{MT}}\}} + \chi_{\{Q(t)<0\}} \chi_{\{\mathbf{x} \in \Gamma^{\mathrm{AO}}\}} \right), \qquad \xi(\mathbf{x}, t) \qquad = \qquad 10^4 \left(\chi_{\{Q(t)>0\}} \chi_{\{\mathbf{x} \in \Gamma^{\mathrm{AO}}\}} \right.$
$+\chi_{\{Q(t)<0\}} \chi_{\{\mathbf{x} \in \Gamma^{\mathrm{MT}}\}} \left. \right) + 10^1 \left(\chi_{\{Q(t)>0\}} \chi_{\{\mathbf{x} \in \Gamma^{\mathrm{MT}}\}} + \chi_{\{Q(t)<0\}} \chi_{\{\mathbf{x} \in \Gamma^{\mathrm{AO}}\}} \right)$ and $\widetilde{\alpha^{\mathrm{MT}}} = 100$. Indeed, a positive flowrate $(Q(t) > 0)$ corresponds to the LV filling phase in which the mitral valve is

open and the aortic one is closed; conversely, a negative flowrate ($Q(t) < 0$) characterizes the LV ejection phase, with the aortic valve open and the mitral closed. The numerical results are shown at the time instances indicated in Fig. 4a.

In Fig. 4c, we report the evolution of the computed phase-averaged pressure field $\overline{p}(t)$ during the heartbeat, which is defined as:

$$\overline{p}(\mathbf{x}, t) = \frac{1}{N_{\text{av}}} \sum_{j=0}^{N_{\text{av}}-1} p(\mathbf{x}, t + jT_{\text{HB}}). \tag{4.1}$$

Here and in the following, we set $N_{\text{av}} = 7$, corresponding to the last 7 heartbeats of the simulation. The simulated blood flow in the idealized healthy 3D LV of Fig. 4b is visualized in Fig. 5 by considering the phase-averaged velocity field $|\overline{u}|$ defined as:

$$\overline{u}(\mathbf{x}, t) = \frac{1}{N_{\text{av}}} \sum_{j=0}^{N_{\text{av}}-1} u(\mathbf{x}, t + jT_{\text{HB}}). \tag{4.2}$$

Moreover, due to the complexity of the blood flow, the velocity vector $\overline{u}_{\text{plane}}$ (the projection of $\overline{u}$ over the planes) is visualized in Figs. 6-7 over the planes through the LV as reported in Fig. 4b, specifically, we consider the XZ and YZ planes passing through the origin (the center of the ellipsoid representing the LV) and the XY plane passing through the point $(0, 0, -3)^T$ cm. The velocity projected over the planes is visualized with different color scales with respect to the one of Fig. 5.

At the beginning of the diastole, when the LV dilates and is filled with blood entering from the left atrium through the mitral valve, the velocity field inside the LV has a relatively small magnitude. The latter progressively increases in correspondence of the inflow jet through the mitral valve at the E-wave peak. At $t = 0.13$ s, two recirculating regions start to form, as we can see in Fig. 6 for both the XZ and YZ planes. However, as the time advances, the flow behaviour in these planes progressively differentiates. Specifically, at $t = 0.23$ s a large recirculation zone occupying the whole LV cavity can be observed in the XZ plane, in agreement with what reported in [16, 24], as well as a smaller region near the LV apex which is visible during the entire diastolic phase. At the same time, the flow pattern through the YZ plane shows a nearly symmetric behaviour with two small vortexes which progressively interact and give rise to a complex flow pattern. By referring again to the XZ plane, we observe that the recirculating region – shortly after the A-wave – progressively moves to the left side of the plane, i.e. from the LV center to the septum wall, in agreement to [16], allowing the flow to correctly and naturally redirect towards the aortic valve in view of the ejection at systole. At the systolic phase the aortic valve opens, while the mitral valve closes. During the entire systole, the highest velocity magnitude is detected near the aortic valve orifice and small recirculation regions are observed in the whole cavity; moreover, the vortical structures are expelled from the LV and the flow is progressively regularized.

The analysis of the flow through the XY plane emphasises the swirling motion of the fluid, which we further investigate through both the phase-averaged vorticity $\overline{\omega} = \nabla \times \overline{u}$ and the phase-averaged Q-criterion, say $\overline{Q}$-criterion. The latter detects the regions of positive values of the second invariant of the velocity gradient tensor where:

$$\overline{Q} = \frac{1}{2}\left(\|\overline{X}\|_2^2 - \|\overline{S}\|_2^2\right) > 0, \quad \text{with } \overline{X} = \frac{1}{2}\left(\nabla\overline{u} - \nabla\overline{u}^T\right) \text{and } \overline{S} = \frac{1}{2}\left(\nabla\overline{u} + \nabla\overline{u}^T\right); \tag{4.3}$$

see e.g. [41, 72]. In Fig. 8, we show the volume rendering of the phase-averaged vorticity magnitude $\overline{\omega}$ (Hz). We observe that, at the beginning of the diastolic phase, the blood flow exhibits small values

of vorticity in the entire cavity until the strong jet through the mitral valve at the peak E-wave interacts with the quiescent fluid and the shear layer forms a vortex ring [16, 24]. The latter grows in size and is determined by high values of vorticity in the diastolic phase, visible in Figs. 5d-5e. The part of the vortex ring interacting with the LV wall leads to its quick dissipation; however, several small vortexes of medium intensity remain and fill the whole LV cavity during the remaining part of the diastolic phase. The decrement of the inlet flow intensity determines the dissipation of the smallest vortex structures by viscous dissipation mechanisms, with a progressive decay of vorticity magnitude in the entire LV. In the systolic phase, we observe small values of vorticity, while high values are instead detected in proximity of the aortic valve at the peak of the systolic phase. This behaviour, which is in agreement with the numerical results in literature [16, 59, 82], is due to the narrowing of the LV for which the blood is ejected through the aortic valve at high pressure values. The vorticity decreases in the entire cavity at this stage. In order to better highlight the vortex structures, we report in Fig. 9 the phase-averaged $\overline{Q}$-criterion. Specifically, the vortex ring developing at the mitral valve at the early diastole is clearly visible in Fig. 9, where we can also observe its motion toward the apex and its break up into smaller vortex structures that almost completely fill the LV cavity during the diastolic phase and progressively decay, until the beginning of the systolic phase, when these are convected and stretched toward the aortic valve by assuming an elongated shape [16].
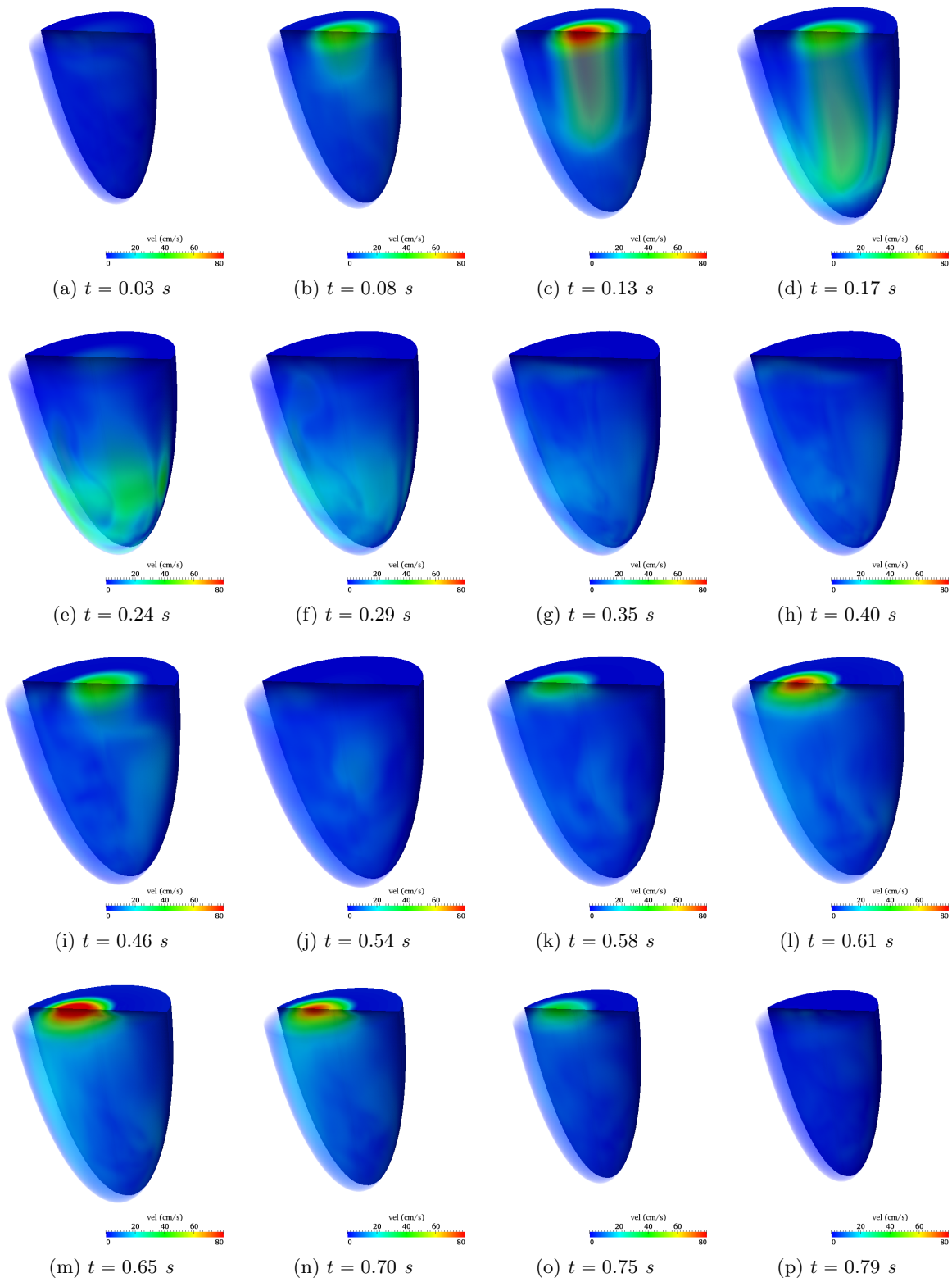
The presence of unsteady vortexes at several spatial scales, their mutual interactions, the rapid variation of the velocity magnitude through the different phases of the heartbeat, and high Reynolds number, yield a fluid regime varying from laminar to transitional, or eventually turbulent. A useful indicator to detect both the transitional nature of the fluid varying from laminar to nearly turbulent over each heartbeat and the cycle-to-cycle variations is the fluctuating kinetic energy (E_{FKE}) which is defined as:

$$E_{\mathrm{FKE}} = \frac{1}{2} \left| \boldsymbol{u}_{\mathrm{rms}}(\mathbf{x}, t) \right|^2,\qquad(4.4)$$

where:

$$\boldsymbol{u}_{\mathrm{rms}}(\mathbf{x}, t) = \sqrt{\overline{\boldsymbol{u}^2}(\mathbf{x}, t) - \bar{\boldsymbol{u}}^2(\mathbf{x}, t)}\qquad(4.5)$$

is the *root mean square velocity*. In Fig. 10, we report the energy E_{FKE} in the LV during the entire heartbeat. We observe that at the beginning of the diastolic phase, E_{FKE} assumes very small values in the whole LV cavity. Then, the formation of the vortex ring at the mitral valve causes the increment of E_{FKE}. However the peak value of E_{FKE} occurs during the decelerating phase between the E- and A-waves, showing that the interaction of the vortex ring with the wall and its disruption into smaller vortex structures causes high velocity fluctuations in the LV, large cycle-to-cycle variations, and eventually may lead to transition to turbulence. Specifically, the largest values of E_{FKE} are obtained in the core of the recirculating zone [16]. The regularization of the flow occurring at the systolic phase corresponds to smaller values of E_{FKE} in the whole LV, although we notice two regions, corresponding to the aortic valve and the recirculating region in the center of the cavity, where the E_{FKE} assumes non-negligible values also at the peak of the outflow flowrate.

(a) $t = 0.03\ s$ (b) $t = 0.08\ s$ (c) $t = 0.13\ s$ (d) $t = 0.17\ s$

(e) $t = 0.24\ s$ (f) $t = 0.29\ s$ (g) $t = 0.35\ s$ (h) $t = 0.40\ s$

(i) $t = 0.46\ s$ (j) $t = 0.54\ s$ (k) $t = 0.58\ s$ (l) $t = 0.61\ s$

(m) $t = 0.65\ s$ (n) $t = 0.70\ s$ (o) $t = 0.75\ s$ (p) $t = 0.79\ s$

Figure 5: Phase-averaged velocity magnitude $|\overline{\boldsymbol{u}}|$ (cm/s) at different times of the heartbeat (Fig. 4a).
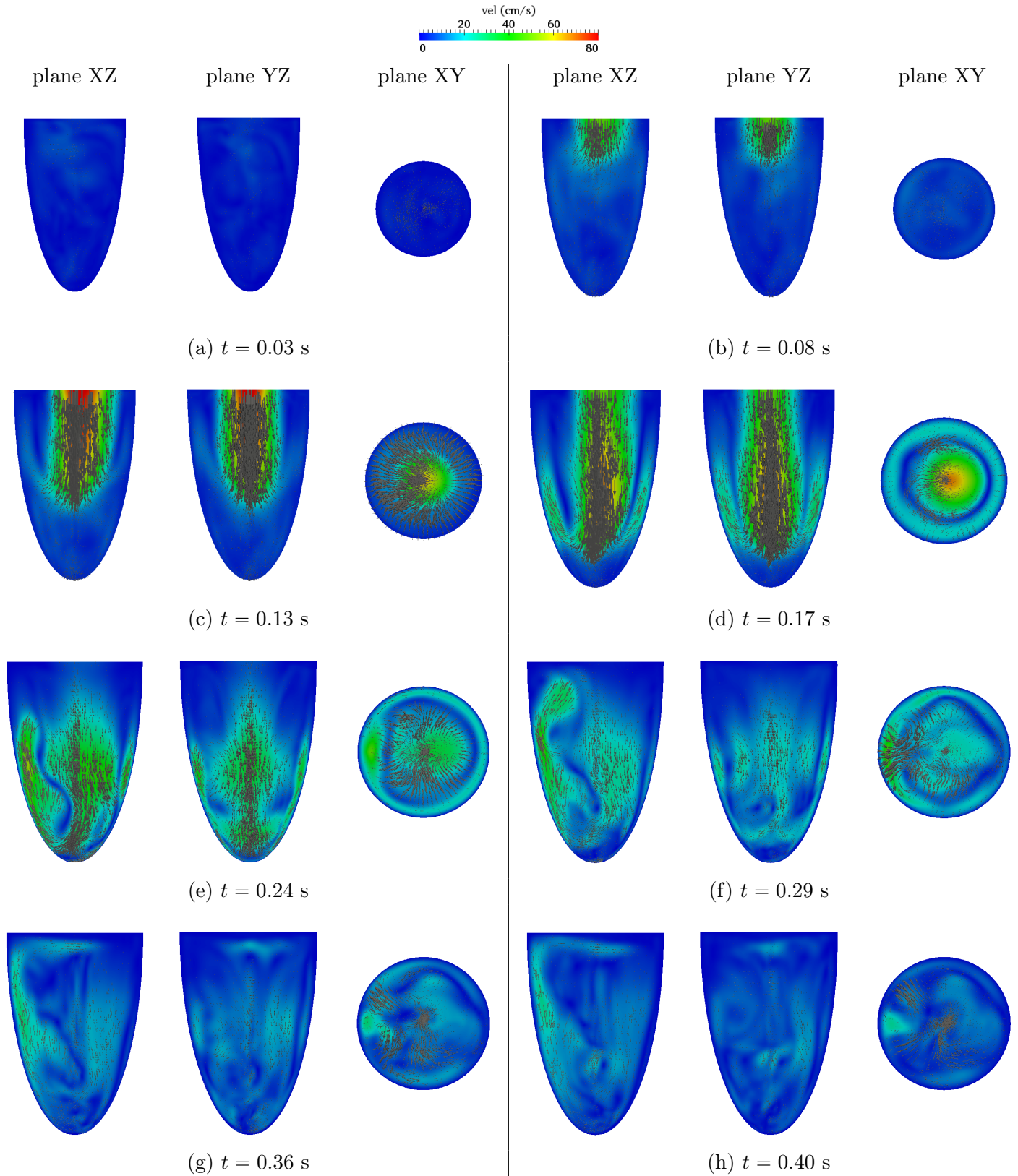
Figure 6: Velocity magnitude $|\overline{\boldsymbol{u}}_{\mathrm{plane}}|$ (cm/s) in the planes XZ, YZ, and XY and at different times. Planes are indicated in Fig. 4b.
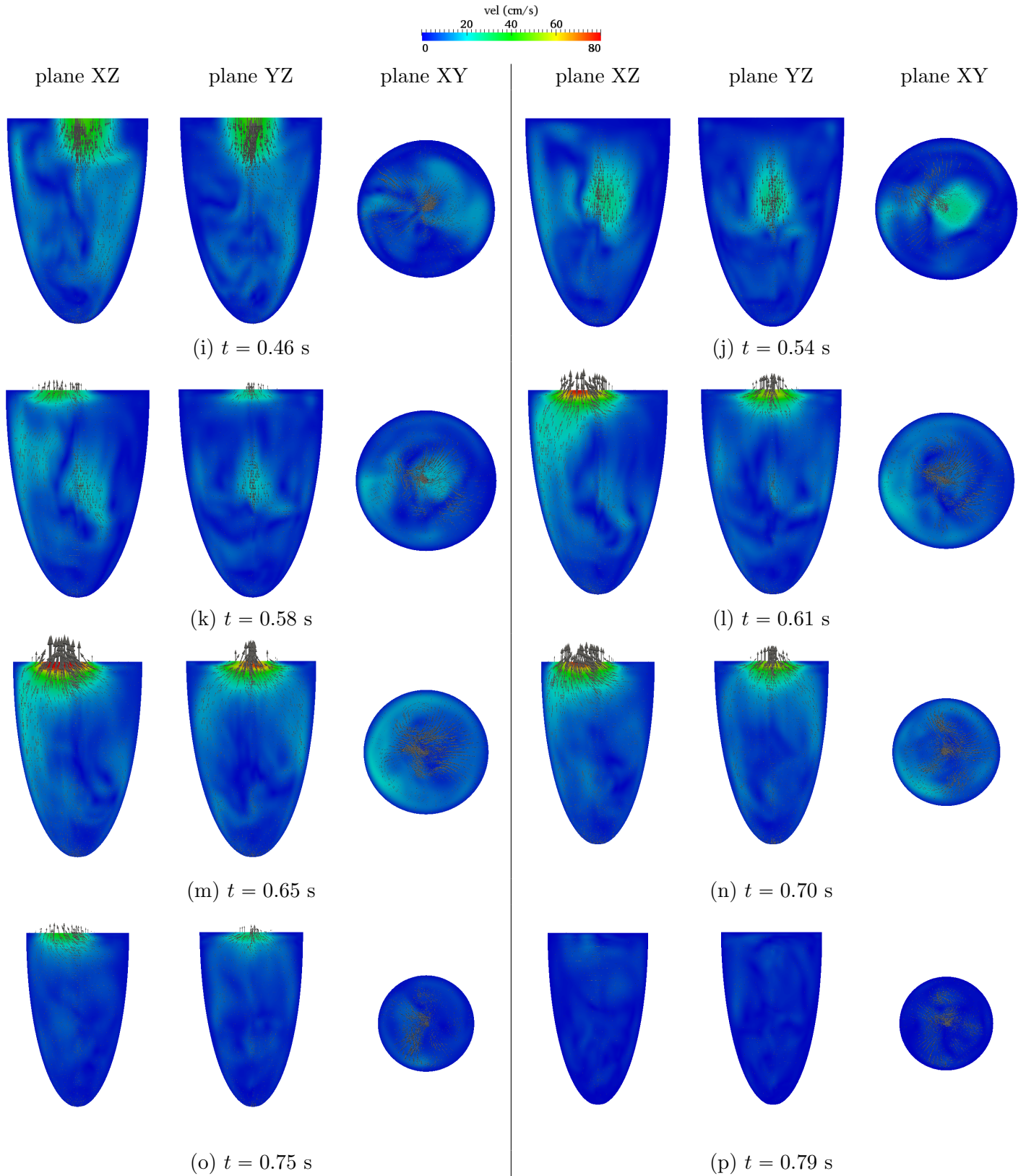
Figure 7: Velocity magnitude $|\overline{\boldsymbol{u}}_{\text{plane}}|$ (cm/s) in the planes XZ, YZ, and XY and at different times. Planes are indicated in Fig. 4b.
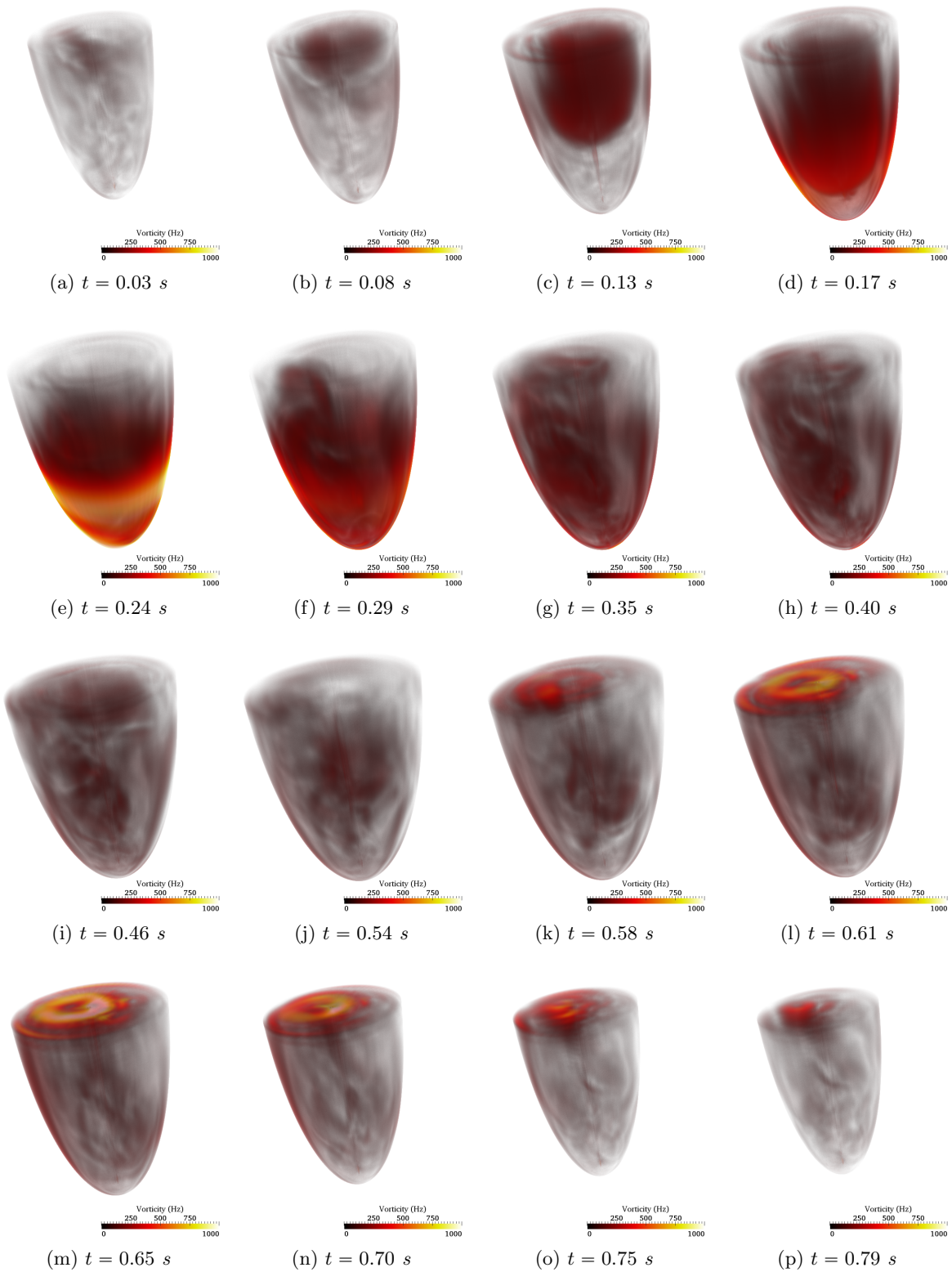
Figure 8: Volume rendering of the phase-averaged vorticity magnitude $|\overline{\boldsymbol{\omega}}|$ (Hz) at different times of the heartbeat (Fig. 4a).
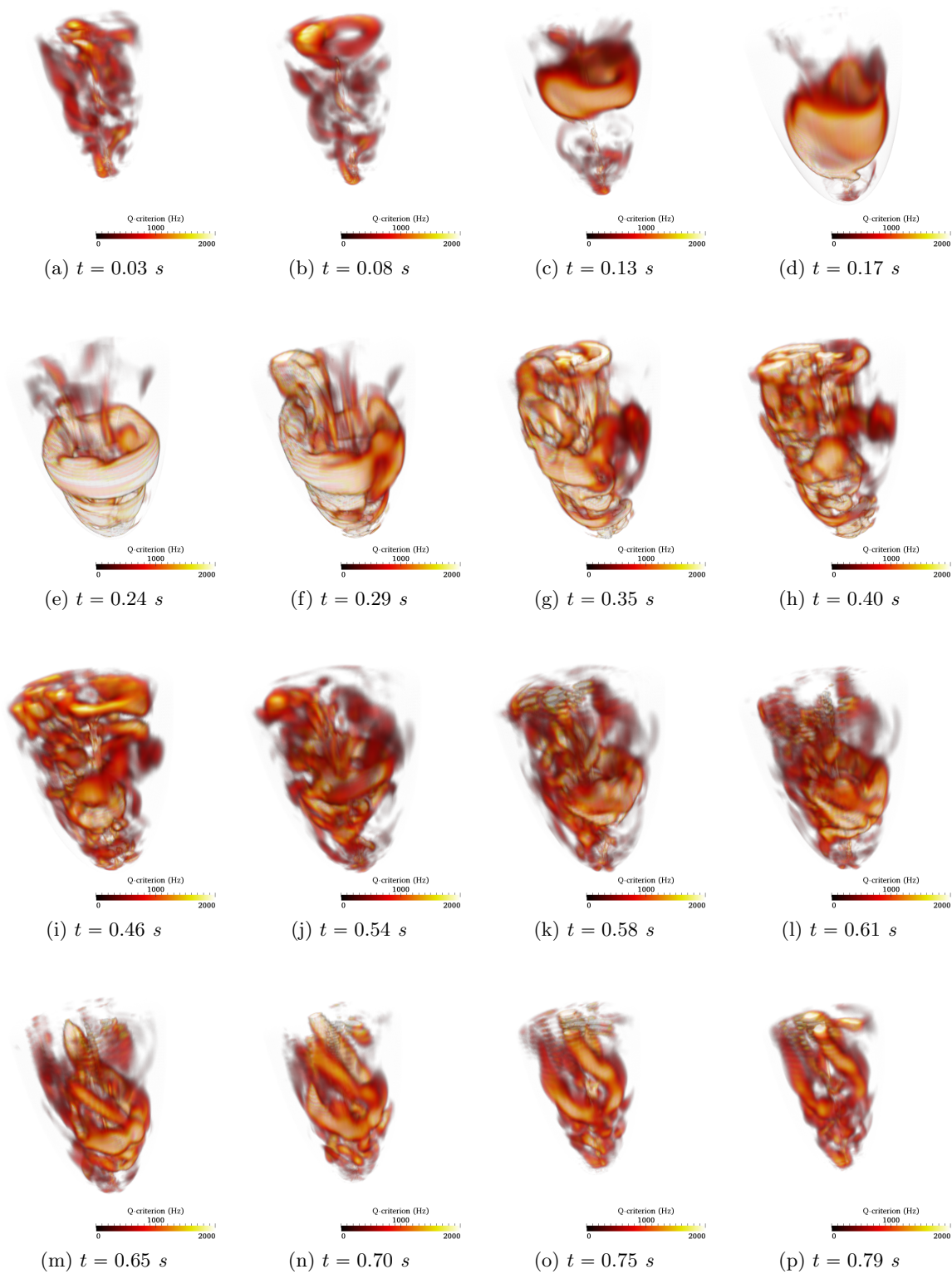
Figure 9: Volume rendering of the phase-averaged $\overline{Q}$-criterion (Hz) at different times of the heartbeat (Fig. 4a).
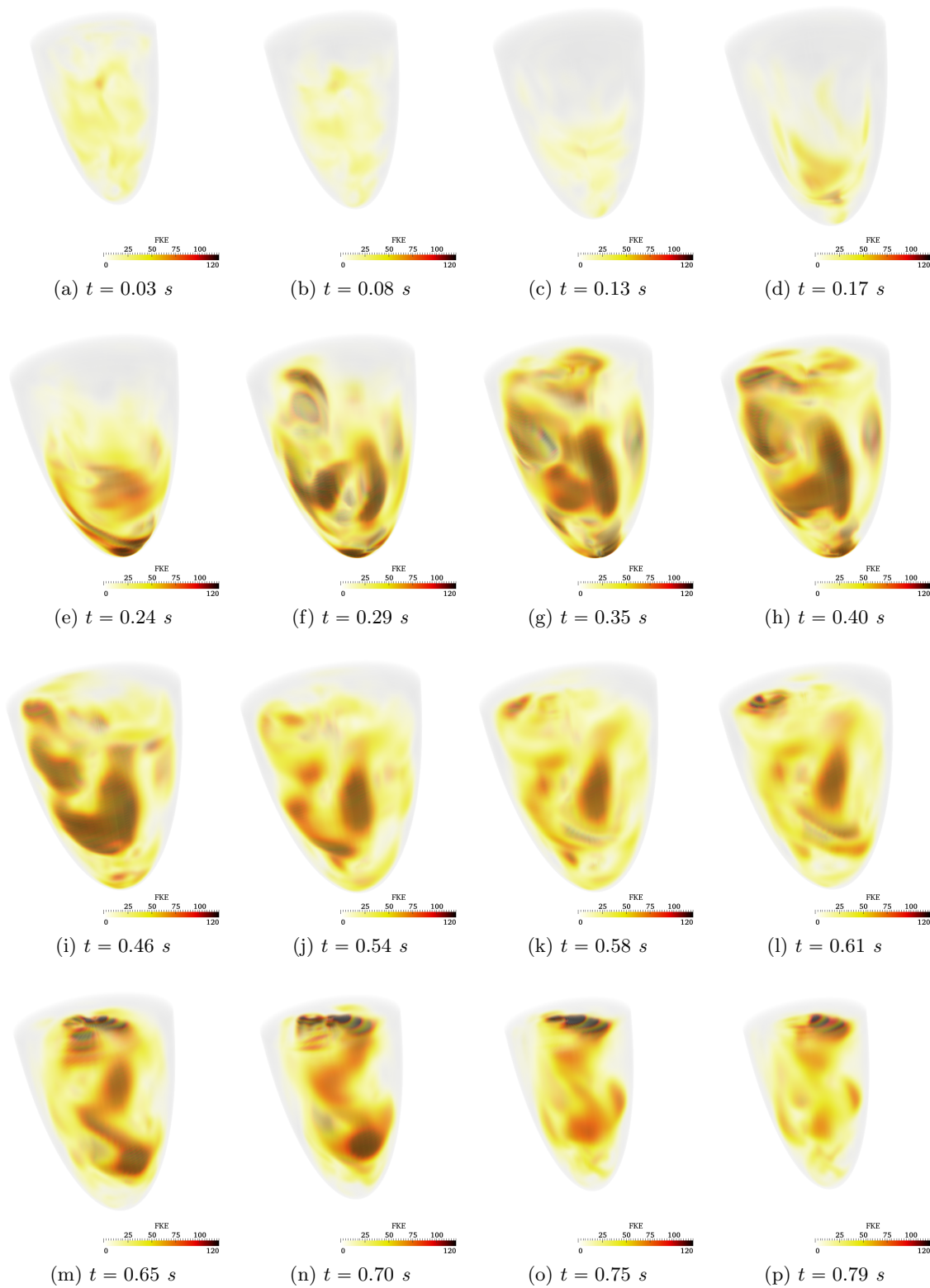
(a) $t = 0.03\ s$ (b) $t = 0.08\ s$ (c) $t = 0.13\ s$ (d) $t = 0.17\ s$

(e) $t = 0.24\ s$ (f) $t = 0.29\ s$ (g) $t = 0.35\ s$ (h) $t = 0.40\ s$

(i) $t = 0.46\ s$ (j) $t = 0.54\ s$ (k) $t = 0.58\ s$ (l) $t = 0.61\ s$

(m) $t = 0.65\ s$ (n) $t = 0.70\ s$ (o) $t = 0.75\ s$ (p) $t = 0.79\ s$

Figure 10: Volume rendering of the fluctuating kinetic energy E_{FKE} ($\mathrm{cm}^2/\mathrm{s}^2$) at different times of the heartbeat (Fig. 4a).

(a) $E_{\mathrm{K}}(t)$ (b) $\rho_{E_{\mathrm{K}}}(t)$
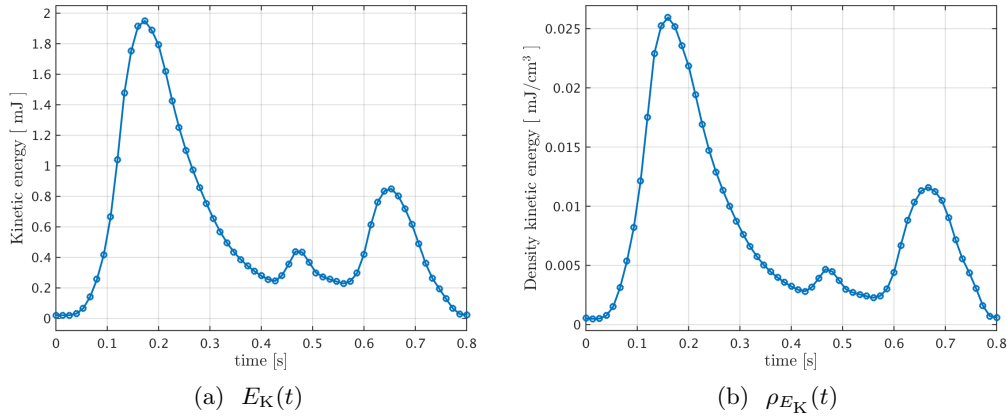
Figure 11: Kinetic energy E_{K} ([mJ]) and density of the kinetic energy $\rho_{E_{\mathrm{K}}}$ ([mJ/cm^3]) vs. time.

We consider additional indicators for the study of the blood flow, specifically the *total kinetic energy* and the *enstrophy* in the LV (see Figs. 11-12). The kinetic energy E_{K} is largely used as indicator of diastolic dysfunction or heart failure in clinical diagnosis; see [45] and references therein. We report in Figs. 11a and 11b the computed kinetic energy E_{K} and density of the kinetic energy $\rho_{E_{\mathrm{K}}}$ vs. time, which are defined as

$$E_{\mathrm{K}}(t) = \frac{1}{2}\rho \int_{\Omega(t)} |\boldsymbol{u}|_2^2 \ \mathrm{d}\Omega \qquad \text{and} \qquad \rho_{E_{\mathrm{K}}}(t) = \frac{E_{\mathrm{K}}(t)}{V(t)}, \tag{4.6}$$

respectively, for all $t \in (0, T)$, where $V(t)$ is the LV volume. The behaviour of the kinetic energy E_{K} reported in Fig. 11a is in full qualitative agreement with that reported in [45] for experimental results obtained from patient-specific 4D CT scans. With respect to [45], the computed values of E_{K} are underestimated by a factor about three, probably due to the different domains (idealized vs. patient-specific) under consideration and the inclusion of the aortic valve root. By considering both Figs. 11a and 11b, we observe that the largest values of these quantities are achieved shortly after the peak E-wave, because the kinetic energy of the blood is stored inside the primary vortex developing in the cavity following the interaction of the jet coming from the mitral valve with the quiescent fluid in the LV. The relatively small variation of the kinetic energy over the heartbeat is an indicator of the fact that the blood flow does not assume a fully turbulent regime which would instead yield a significant loss of energy.

Finally, we report the behaviour of the enstrophy $\mathcal{E}$, as a measure of the total vorticity in the LV, and its density $\rho_{\mathcal{E}}$, defined as

$$\mathcal{E}(t) = \frac{1}{2} \int_{\Omega(t)} |\nabla \times \boldsymbol{u}|_2^2 \ \mathrm{d}\Omega \qquad \text{and} \qquad \rho_{\mathcal{E}}(t) = \frac{\mathcal{E}(t)}{V(t)}, \tag{4.7}$$

respectively, for all $t \in (0, T)$. The results of Figs. 12a and 12b show that, in the late diastole the enstrophy decays slower than the kinetic energy, while, during the systolic phase, more rapidly.

4.2 Results for a prescribed inflow velocity profile at the mitral valve

In Sec. 2.4.2, we stressed the fact that the treatment of the mitral valve and specifically the inflow velocity profile has a crucial role on the blood flow patterns developed in the LV. In this section, we
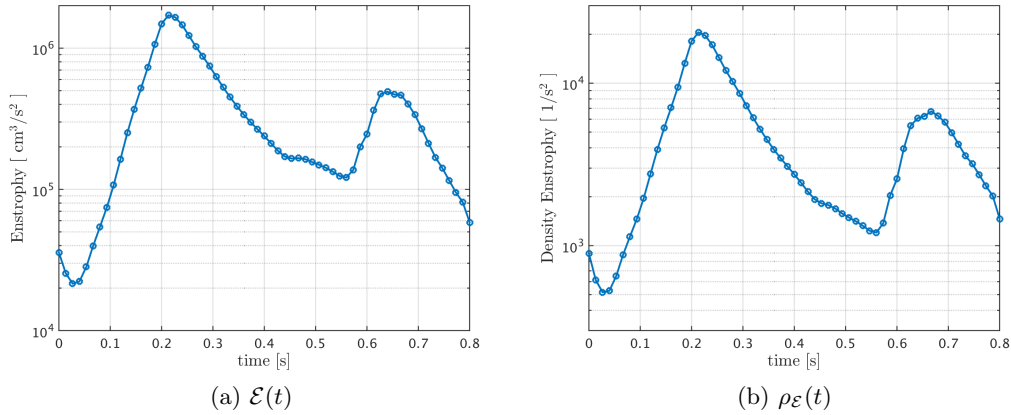
(a) $\mathcal{E}(t)$ (b) $\rho_{\mathcal{E}}(t)$

Figure 12: Enstrophy $\mathcal{E}$ ([cm^3/s^2]) and density of the enstrophy $\rho_{\mathcal{E}}$ ([1/s^2]) vs. time.

compare the blood flow patterns obtained in Sec. 4.1 with those obtained by a prescribed Dirichlet BCs at the mitral valve weakly set through the ENM. Specifically, we consider the parabolic profile defined in Sec. 2.4.2. In Fig. 13, we report the phase-averaged velocity magnitude $|\overline{\boldsymbol{u}}|$ obtained with the weakly imposed parabolic profile at the mitral valve and, in Figs. 14-15, the corresponding phase-averaged vorticity $|\overline{\boldsymbol{\omega}}|$ and $\overline{Q}$-criterion.

As expected, both the velocity field and the vortexes differ from the case when resistance BCs are instead considered at the mitral valve, especially at the end of the diastolic phase. Moreover, we notice that the different distribution of the flow leads to a larger number of vortex structures in the systolic phase for the prescribed velocity profile than with the MTV BC at the mitral valve. Indeed, by comparing Figs. 15m–15p to Figs. 9m–9p, we observe that the vortex structures fill the entire LV cavity and do not show an elongated shape as in the previous case and as expected in the literature [16, 59, 82]. We conclude that the use of MTV BCs both at the mitral and aortic valves yields more realistic results and allows better characterizations of the blood flow in the LV.
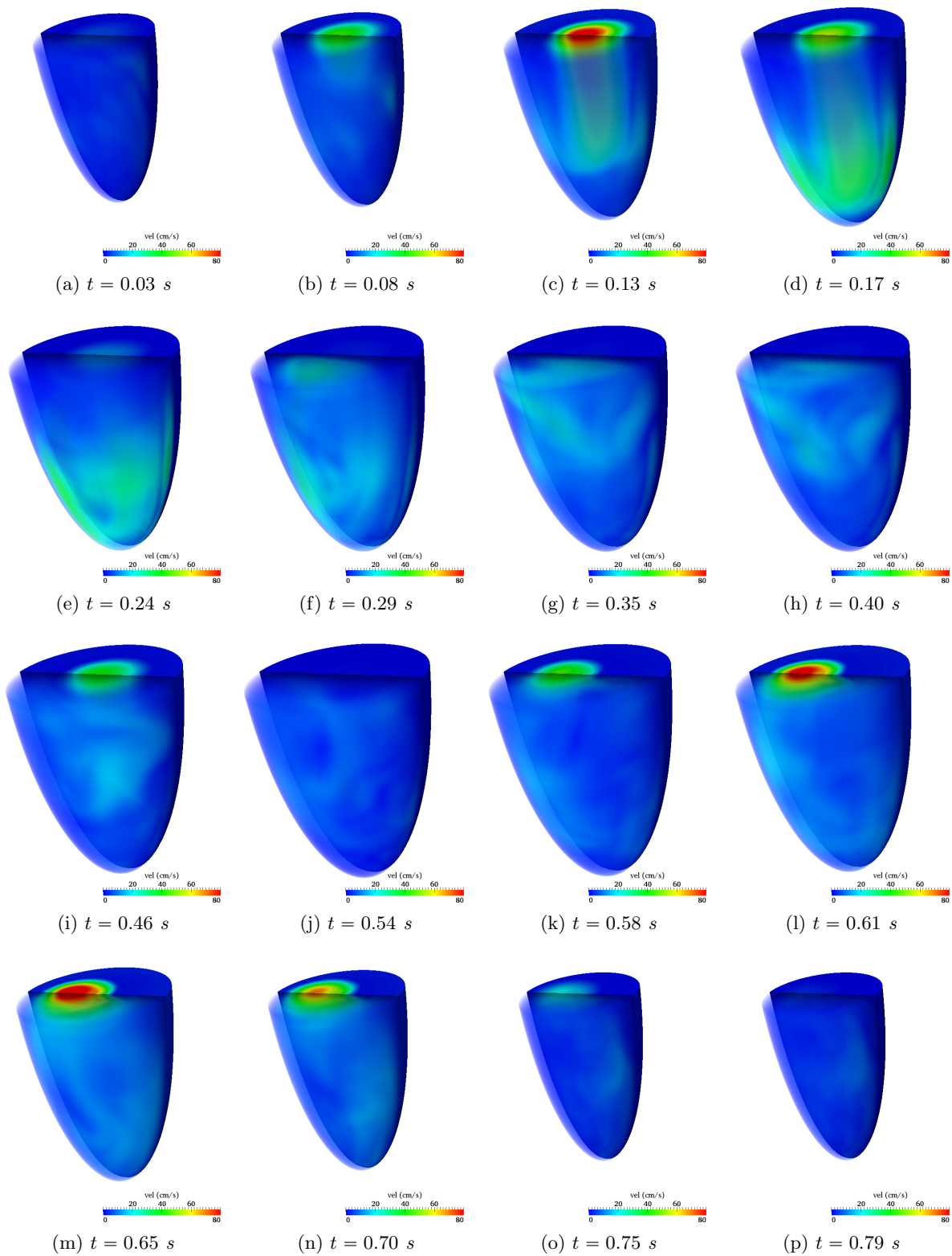
(a) $t = 0.03$ s (b) $t = 0.08$ s (c) $t = 0.13$ s (d) $t = 0.17$ s

(e) $t = 0.24$ s (f) $t = 0.29$ s (g) $t = 0.35$ s (h) $t = 0.40$ s

(i) $t = 0.46$ s (j) $t = 0.54$ s (k) $t = 0.58$ s (l) $t = 0.61$ s

(m) $t = 0.65$ s (n) $t = 0.70$ s (o) $t = 0.75$ s (p) $t = 0.79$ s

Figure 13: Phase-averaged velocity magnitude $|\overline{\boldsymbol{u}}|$ (cm/s) at different times of the heartbeat (Fig. 4a) for a prescribed inflow velocity profile at the mitral valve.
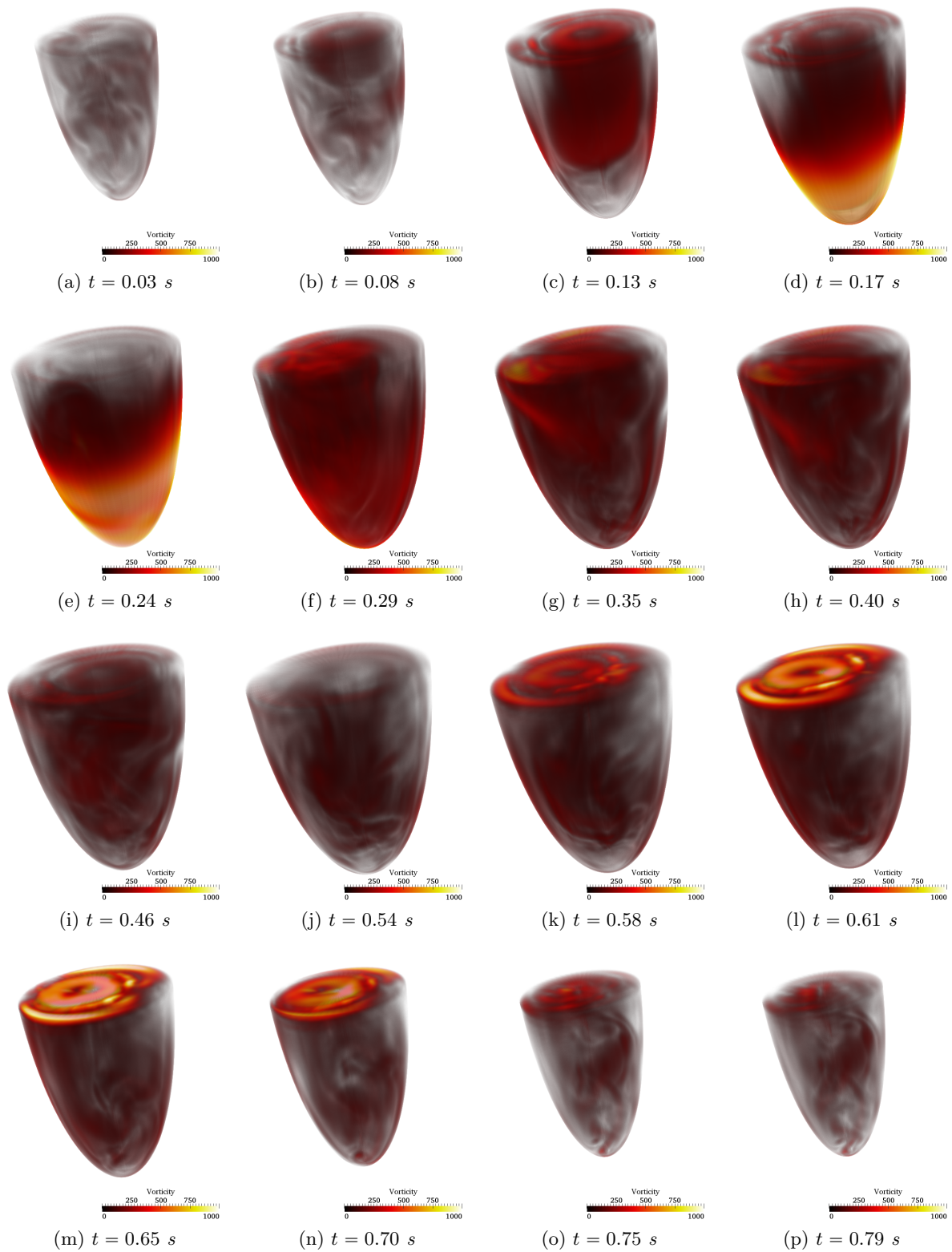
Figure 14: Volume rendering of the phase-averaged vorticity magnitude $|\overline{\boldsymbol{\omega}}|$ (Hz) at different times of the heartbeat (Fig. 4a) for a prescribed inflow velocity profile at the mitral valve.
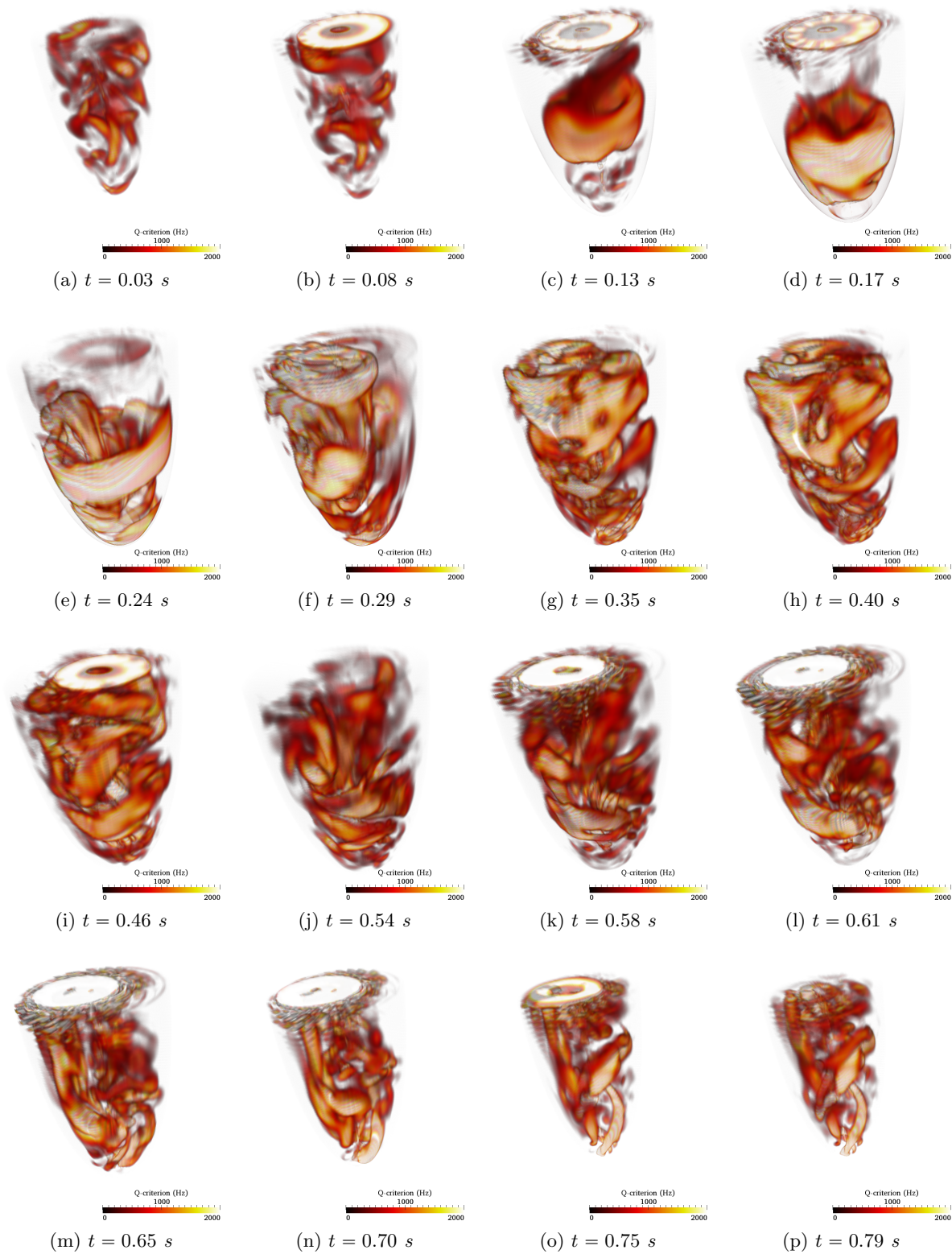
Figure 15: Volume rendering of the phase-averaged $\overline{Q}$-criterion (Hz) at different times of the heartbeat (Fig. 4a) for a prescribed inflow velocity profile at the mitral valve.
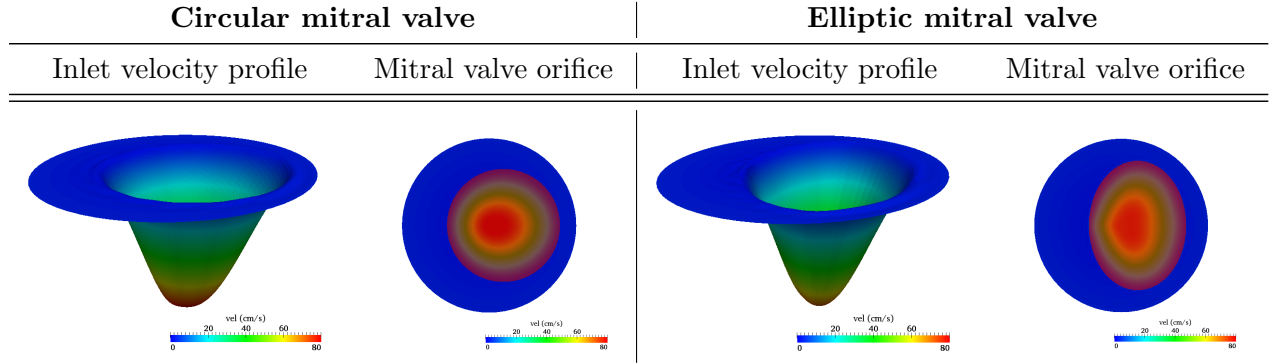
Circular mitral valve		Elliptic mitral valve	
Inlet velocity profile	Mitral valve orifice	Inlet velocity profile	Mitral valve orifice

Figure 16: Comparison between the inflow velocity profiles for the circular (on the left) and elliptic (on the right) mitral valves cases: inflow velocity profiles and highlighting of the prescribed mitral valve orifice at the peak E-wave time ($t = 0.13$ s).

4.3 Results for elliptic mitral valve

We compare the LV blood flow computed in Sec. 4.1 for a circular mitral valve to those obtained by assuming an elliptic shape valve. Specifically, we consider the part of boundary corresponding to the mitral valve as the region:

$$\Gamma^{\mathrm{MT}} = \left\{ (x, y, 0) \in \mathbb{R}^3 : \frac{(x - \boldsymbol{\epsilon}_{\mathrm{MT}}^x)^2}{a_{\mathrm{MT}}^2} + \frac{(y - \boldsymbol{\epsilon}_{\mathrm{MT}}^y)^2}{b_{\mathrm{MT}}^2} = 1, z = 0 \right\}, \qquad (4.8)$$

with $\boldsymbol{\epsilon}_{\mathrm{MT}} = (0.40,\ 0,\ 0)^T$ cm, $b_{\mathrm{MT}} = 1.60$ cm and $a_{\mathrm{MT}} = \frac{3}{4} b_{\mathrm{MT}}$, such that the mitral valve area is equal to the circular case. We highlight that in both cases we consider MTV BC with the regularization of Sec. 2.4.2 for the mitral valve.

In Fig. 16, we compare the inflow velocity profiles obtained at the peak diastolic phase. Moreover, we observe that, for the elliptic mitral valve, the velocity assumes smaller values, being the inflow profile flatter than the one obtained in the circular orifice. Indeed, for the elliptic mitral valve the velocity magnitude inside the cavity is smaller during the whole diastolic phase, as can be observed by comparing Fig. 17 to Fig. 5, in terms of the phase-averaged velocity $|\overline{\boldsymbol{u}}|$.

In order to better highlight the differences in the flow patterns inside the LV cavity, we also report in Figs. 18-19 the velocity vector $\overline{\boldsymbol{u}}_{\mathrm{plane}}$ visualized over the planes through the LV as reported in Fig. 4b. Besides the intensity of the inflow jet, the most significant differences during the diastolic phase can be observed at time $t = 0.23$ s where the recirculation region occupies a smaller area and the velocity near the left ventricular wall assumes smaller values than with a circular orifice. Moreover, we notice that the symmetry of the velocity field in the YZ plane is lost earlier in the circular case. The different flow pattern inside the cavity during the diastolic phase causes a different distribution of the flow at the beginning of the systolic phase when the velocity assumes smaller values (see Fig. 17l and Fig. 5l). Moreover, in Fig. 19 we observe that at $t = 0.65$ s the small recirculation region is located closer to the right wall.

In Figs. 20 and 21, we report the computed phase-averaged vorticity $|\overline{\boldsymbol{\omega}}|$ and the $\overline{Q}$-criterion, respectively. We notice that the vorticity exhibit a similar behaviour to the case of the circular mitral valve (Fig. 8). However, differences in the intensity of the inflow jet cause the development of a vortex ring that, albeit of similar shapes, is less intense; moreover, the vortex structures developing at late diastole are significantly different too. In the systolic phase, however, we observe a similar

behaviour of the vortex structures which are convected toward the aortic valve with elongated shapes.
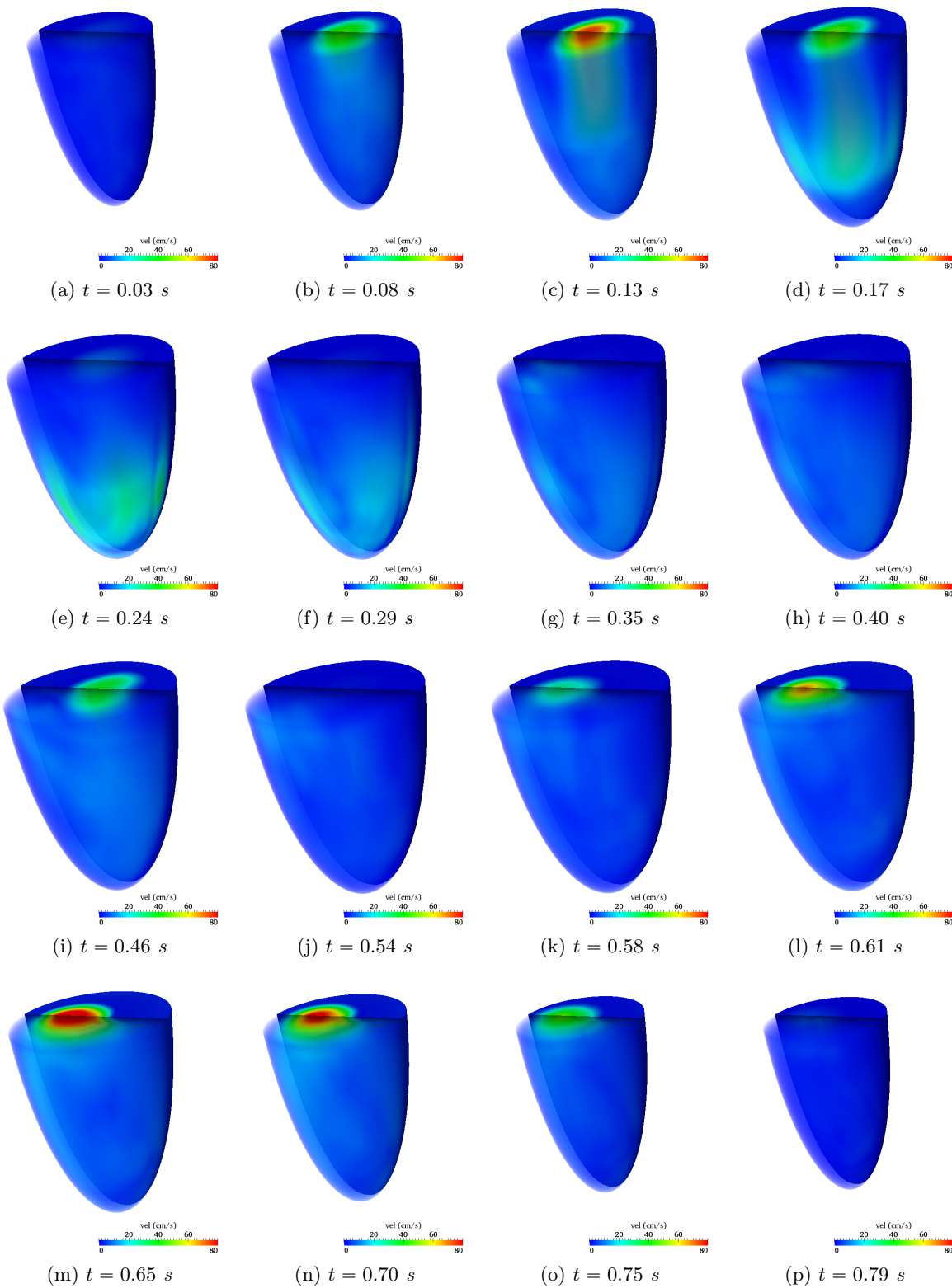
(a) $t = 0.03\ s$ (b) $t = 0.08\ s$ (c) $t = 0.13\ s$ (d) $t = 0.17\ s$

(e) $t = 0.24\ s$ (f) $t = 0.29\ s$ (g) $t = 0.35\ s$ (h) $t = 0.40\ s$

(i) $t = 0.46\ s$ (j) $t = 0.54\ s$ (k) $t = 0.58\ s$ (l) $t = 0.61\ s$

(m) $t = 0.65\ s$ (n) $t = 0.70\ s$ (o) $t = 0.75\ s$ (p) $t = 0.79\ s$

Figure 17: Phase-averaged velocity magnitude $|\overline{\boldsymbol{u}}|$ (cm/s) at different times of the heartbeat (Fig. 4a) for the elliptic mitral valve.

plane XZ   plane YZ   plane XY   plane XZ   plane YZ   plane XY

(a) $t = 0.02$ s

(b) $t = 0.08$ s

(c) $t = 0.13$ s

(d) $t = 0.17$ s

(e) $t = 0.24$ s

(f) $t = 0.29$ s

(g) $t = 0.35$ s

(h) $t = 0.40$ s
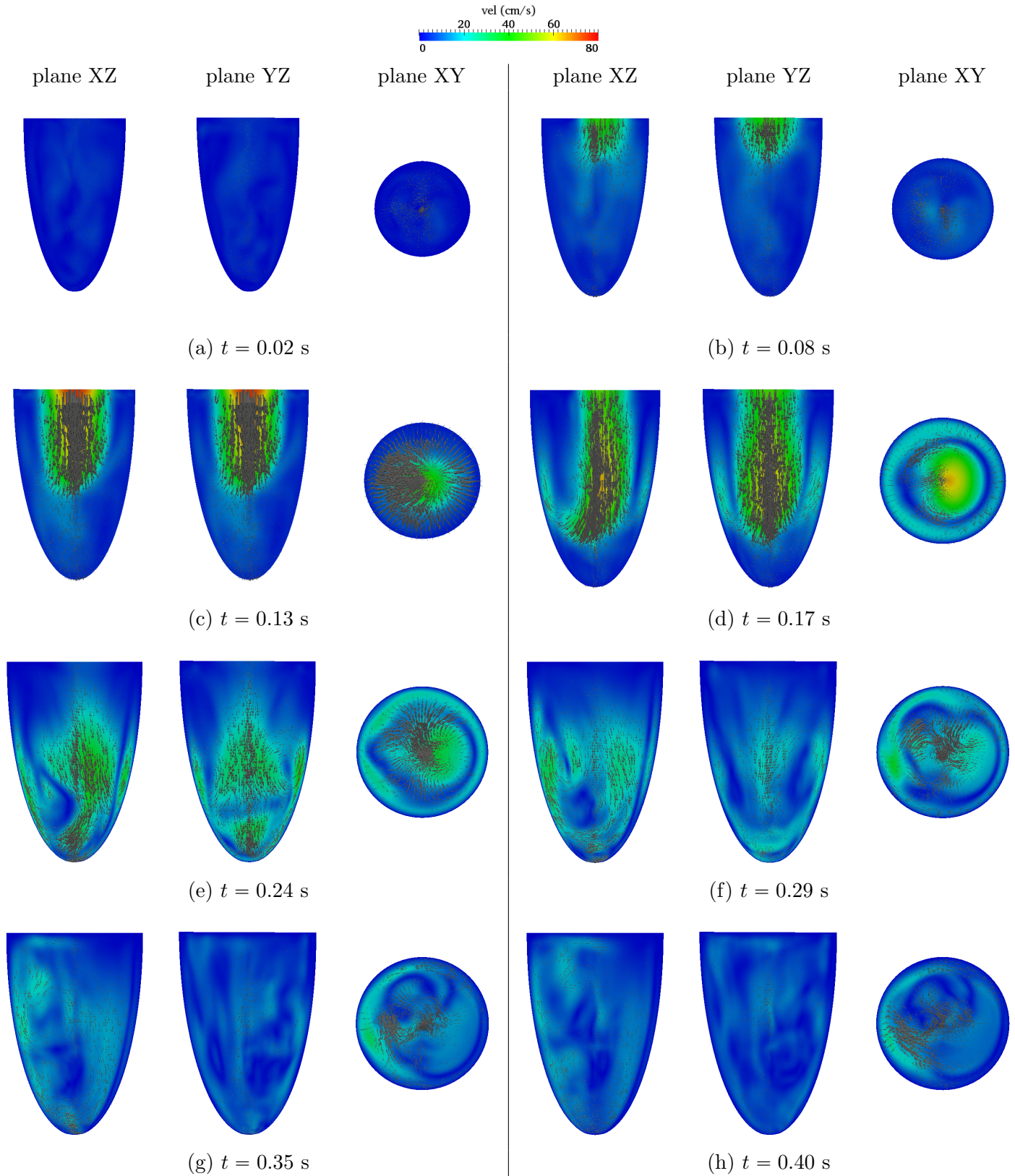
Figure 18: Velocity magnitude $|\overline{\boldsymbol{u}}_{\mathrm{plane}}|$ (cm/s) in the planes XZ, YZ, and XY and at different times for the elliptic mitral valve. Planes are indicated in Fig. 4b.
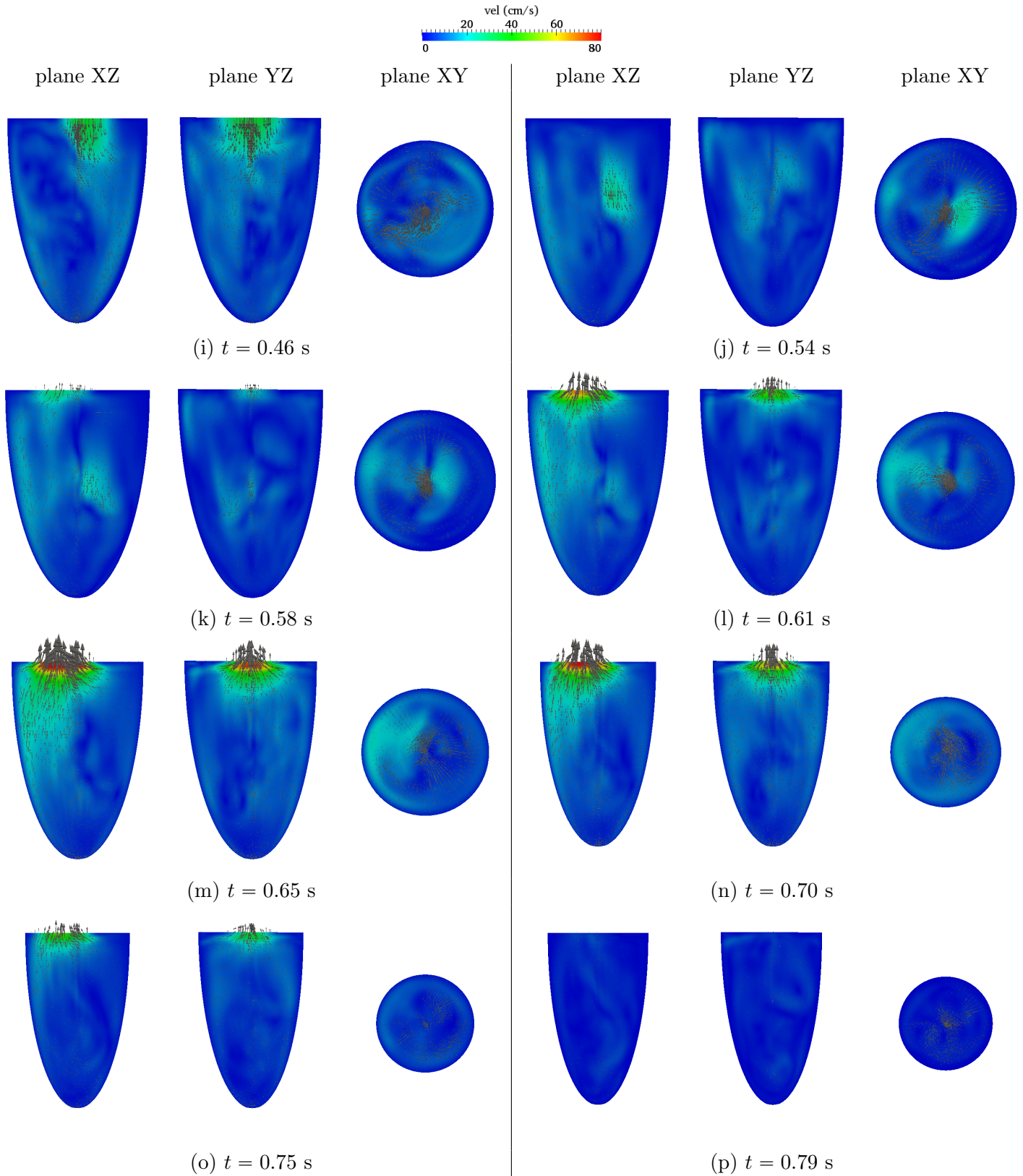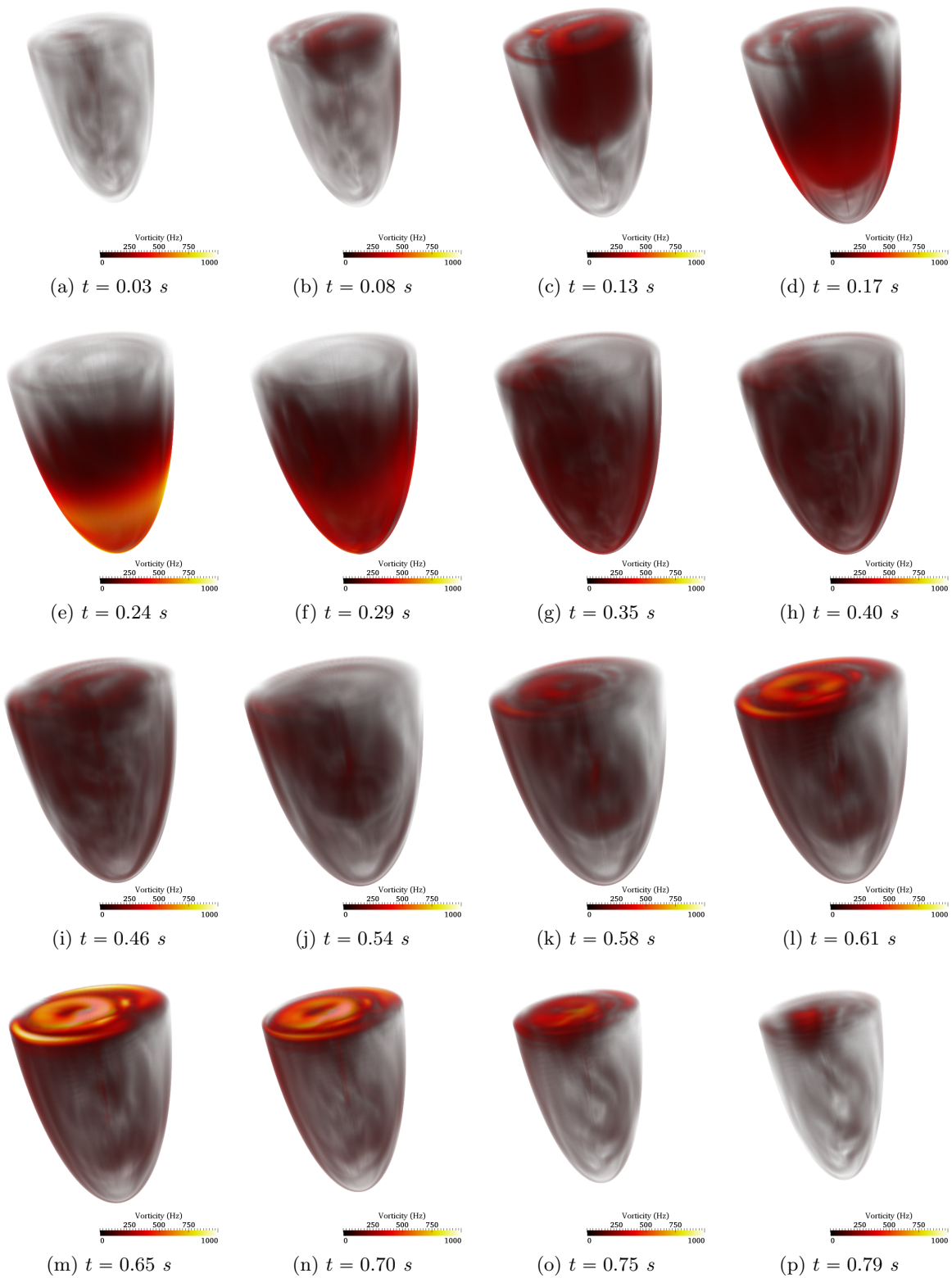
Figure 19: Velocity magnitude $|\overline{\boldsymbol{u}}_{\text{plane}}|$ (cm/s) in the planes XZ, YZ, and XY and at different times for the elliptic mitral valve. Planes are indicated in Fig. 4b.

Figure 20: Volume rendering of the phase-averaged vorticity magnitude $|\overline{\boldsymbol{\omega}}|$ (Hz) at different times of the heartbeat (Fig. 4a) for the elliptic mitral valve.
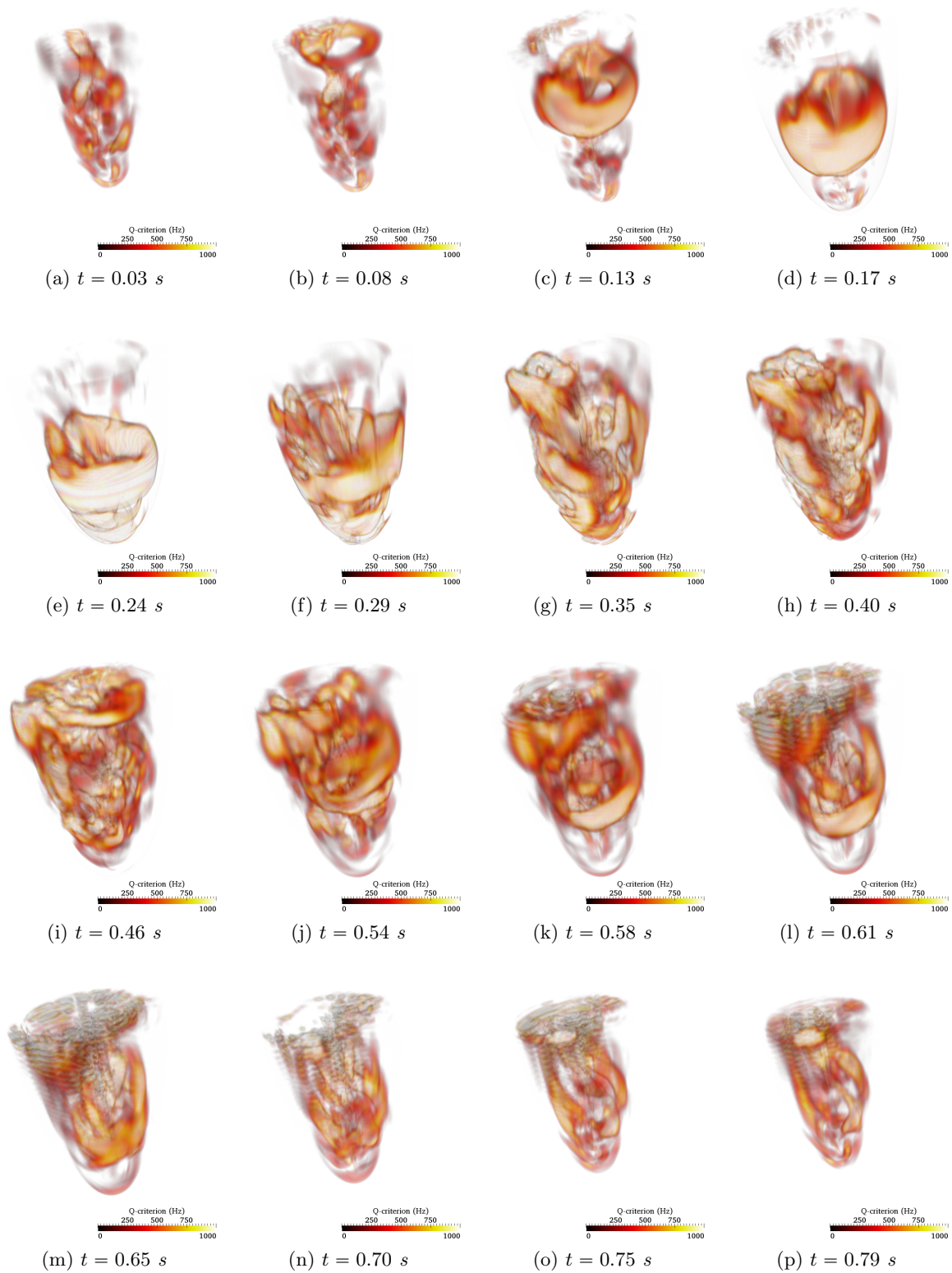
(a) $t = 0.03\ s$ (b) $t = 0.08\ s$ (c) $t = 0.13\ s$ (d) $t = 0.17\ s$

(e) $t = 0.24\ s$ (f) $t = 0.29\ s$ (g) $t = 0.35\ s$ (h) $t = 0.40\ s$

(i) $t = 0.46\ s$ (j) $t = 0.54\ s$ (k) $t = 0.58\ s$ (l) $t = 0.61\ s$

(m) $t = 0.65\ s$ (n) $t = 0.70\ s$ (o) $t = 0.75\ s$ (p) $t = 0.79\ s$

Figure 21: Volume rendering of the phase-averaged $\overline{Q}$-criterion (Hz) at different times of the heartbeat (Fig. 4a) for the elliptic mitral valve.
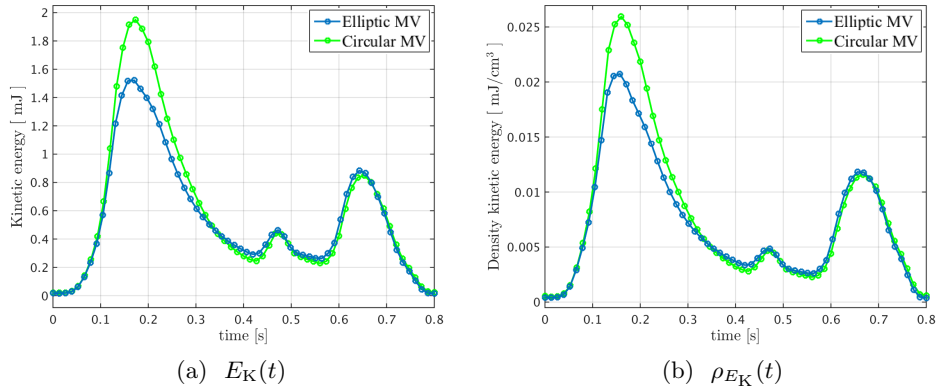
(a) $E_{\mathrm{K}}(t)$ (b) $\rho_{E_{\mathrm{K}}}(t)$

Figure 22: Kinetic energy E_{K} ([mJ]) and density of the kinetic energy $\rho_{E_{\mathrm{K}}}$ ([mJ/cm^3]) vs. time for the elliptic mitral valve.

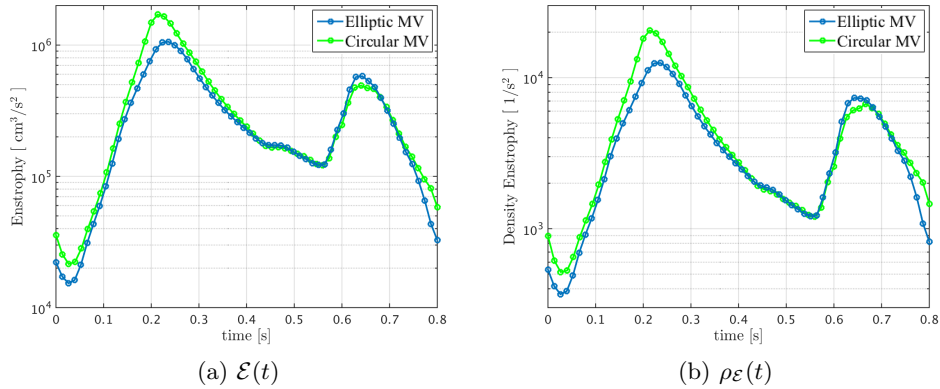(a) $\mathcal{E}(t)$ (b) $\rho_{\mathcal{E}}(t)$

Figure 23: Enstrophy $\mathcal{E}$ ([cm^3/s^2]) and density of the enstrophy $\rho_{\mathcal{E}}$ ([1/s^2]) vs. time for the elliptic mitral valve.

Both the kinetic energy $E_{\mathrm{K}}(t)$ (Fig. 22) and the enstrophy $\mathcal{E}(t)$ (Fig. 23), show qualitatively a similar behaviour, even if the peak value of E_{K}, corresponding to the E-wave, for the elliptic valve is smaller than for the circular one (about 25%).

5   Conclusions

In this work, we extensively studied and critically discussed the blood flow in an idealized LV by means of numerical simulations. Our computational approach is based on the treatment of the mitral and aortic valves as MTV BCs of the Navier-Stokes equations; these BCs surrogate the valves' behaviour and allow more realistic blood flow in the LV than with prescribed velocity inflow and outflow profiles. At the numerical level, such MTV BCs are weakly enforced through the ENM yielding a straightforward numerical approach [44, 75, 76]. Our computational study highlights several features of the blood flow in a reference, idealized 3D LV, in particular phase-averaged velocity, vorticity, and vortex structures, as well as fluctuating energy, enstrophy, and total kinetic

energy. In particular, the evolution of the latter provides a precious, synthetic indicator to characterize the LV blood flow along the heartbeat and can be used to highlight abnormal flow behaviours. Our study also clearly evidences that the ventricular blood flow is strongly affected by the inflow at the mitral valve and the shape of this orifice.

References

[1] M. Astorino, J. Hamers, S.C. Shadden, and J.-F. Gerbeau. A robust and efficient valve model based on resistive immersed surfaces. *International Journal for Numerical Methods in Biomedical Engineering*, **28**:937–959, 2012.

[2] B. Baccani, F. Domenichini, and G. Pedrizzetti. Vortex dynamics in a model left ventricle during filling. *European Journal of Mechanics – B/Fluids*, **21**:527–543, 2002.

[3] B. Baccani, F. Domenichini, G. Pedrizzetti, and G. Tonti. Fluid dynamics of the left ventricular filling in dilated cardiomyopathy. *Journal of Biomechanics*, **35**:665–671, 2002.

[4] Y. Bazilevs, L. Beirão da Veiga, J.A. Cottrell, T.J.R. Hughes, and G. Sangalli. Isogeometric Analysis: approximation, stability, and error estimates for h-refined meshes. *Mathematical Models and Methods in Applied Sciences*, **16**:1031–1090, 2006.

[5] Y. Bazilevs, V.M. Calo, J.A. Cottrell, T.J.R. Hughes, A. Reali, and G. Scovazzi. Variational multiscale residual-based turbulence modeling for large eddy simulation of incompressible flows. *Computer Methods in Applied Mechanics and Engineering*, **197**:173–201, 2007.

[6] Y. Bazilevs, V.M. Calo, T.J.R. Hughes, and Y. Zhang. Isogeometric fluid-structure interaction: theory, algorithms and computations. *Computational Mechanics*, **43**:3–37, 2008.

[7] Y. Bazilevs, J.R. Gohean, T.J.R. Hughes, R.D. Moser, and Y. Zhang. Patient-specific Isogeometric fluid-structure interaction analysis of thoracic aortic blood flow due to implantation of the Jarvik 2000 left ventricular assist device. *Computer Methods in Applied Mechanics and Engineering*, **198**:3534–3550, 2009.

[8] Y. Bazilevs and T.J.R. Hughes. Weak imposition of Dirichlet boundary conditions in fluid mechanics. *Computers & Fluids*, **36**:12–26, 2007.

[9] Y. Bazilevs, C. Michler, V.M. Calo, and T.J.R. Hughes. Weak Dirichlet boundary conditions for wall-bounded turbulent flows. *Computer Methods in Applied Mechanics and Engineering*, **196**:4853–4862, 2007.

[10] B.J. Bellhouse. Fluid mechanics of a model mitral valve and left ventricle. *Cardiovascular Research*, **6**:199–210, 1972.

[11] C. Bertoglio and A. Caiazzo. A Stokes-residual backflow stabilization method applied to physiological flows. *Journal of Computational Physics*, **313**:260–278, 2016.

[12] C. Bertoglio and A. Caiazzo. A tangential regularization method for backflow stabilization in hemodynamics. *Journal of Computational Physics*, **261**:162–171, 2014.

[13] F. Brezzi and M. Fortin. *Mixed and Hybrid Finite Element Methods*. Springer–Verlag, New York, 1991.

[14] P. Bogacki and L.F. Shampine. A 3(2) pair of Runge-Kutta formulas. *Applied Mathematics Letters*, **2**:1–9, 1989.

[15] R. Calderer and A. Masud. A multiscale stabilized ALE formulation for incompressible flows with moving boundaries. *Computational Mechanics*, **46**:185–197, 2010.

[16] C. Chnafa, S. Mendez, and F. Nicoud. Image-based large-eddy simulation in a realistic left heart. *Computers & Fluids*, **94**:173–187, 2014.

[17] J. Chung and G.M. Hulbert. A time integration algorithm for structural dynamics with improved numerical dissipation: the generalized-α method. *Journal of Applied Mechanics*, **60**:371–375, 1993.

[18] Ph.G. Ciarlet. *The Finite Element Method for Elliptic Problems*. North–Holland, Amsterdam, 1978.

[19] J.A. Cottrell, T.J.R. Hughes, and Y. Bazilevs. Isogeometric Analysis: CAD, finite elements, NURBS, exact geometry and mesh refinement. *Computer Methods in Applied Mechanics and Engineering*, **194**:4135–4195, 2005.

[20] J.A. Cottrell, T.J.R. Hughes, and Y. Bazilevs. *Isogeometric Analysis: Toward Integration of CAD and FEA*. John Wiley & Sons, Chichester, UK, 2009.

[21] J.A. Cottrell, T.J.R. Hughes, and A. Reali. Studies of refinement and continuity in Isogeometric structural analysis. *Computer Methods in Applied Mechanics and Engineering*, **196**:4160–4183, 2007.

[22] L. Dedè, M.J. Borden, and T.J.R. Hughes. Isogeometric analysis for topology optimization with a phase field model. *Archives of Computational Methods in Engineering*, **19**:427–465, 2012.

[23] F. Domenichini and G. Pedrizzetti. Intraventricular vortex flow changes in the infarcted left ventricle: numerical results in an idealised 3D shape. *Computer Methods in Biomechanics and Biomedical Engineering*, **14**:95–101, 2011.

[24] F. Domenichini, G. Pedrizzetti, and B. Baccani. Three-dimensional filling flow into a model left ventricle, *Journal of Fluid Mechanics*, **539**:179–198, 2005.

[25] F. Domenichini, G. Querzoli, A. Cenedese, and G. Pedrizzetti. Combined experimental and numerical analysis of the flow structure into the left ventricle, *Journal of Biomechanics*, **40**:1988–1994, 2007.

[26] J. Donea. Arbitrary Lagrangian-Eulerian finite element methods. In T.J.R. Hughes and T. Belytschko (Eds.), *Computational Methods for Transient Analysis*, **198**:473–516, 1983.

[27] J. Donea, P. Fasoli-Stella, and S. Giuliani. Lagrangian and Eulerian finite element techniques for transient fluid-structure interaction problems. *Transactions of the 4th SMIRT Conference*, **B**, 1977.

[28] J. Donea, S. Giuliani, and J.P. Halleux. An arbitrary Lagrangian-Eulerian finite element method for transient dynamic fluid-structure interactions. *Computer Methods in Applied Mechanics and Engineering*, **33**:689–723, 1982.

[29] K.S. Dujardin, M. Enriquez-Sarano, A. Rossi, K.R. Bailey, and J.B. Seward. Echocardiographic assessment of left ventricular remodeling: are left ventricular diameters suitable tools? *Journal of the American College of Cardiology*, **30**:1534–1541, 1997.

[30] A. Falahatpisheh and A. Kheradvar. High-speed particle image velocimetry to assess cardiac fluid dynamics in vitro: From performance to validation. *European Journal of Mechanics - B/Fluids*, **35**:2–8, 2012.

[31] M. Fedele, E. Faggiano, L. Dedè, and A. Quarteroni. A patient-specific aortic valve model based on moving resistive immersed implicit surfaces. *MATHICSE report*, 2016.

[32] L. Formaggia and F. Nobile. A stability analysis for the arbitrary Lagrangian Eulerian formulation with finite elements. *East-West Journal of Numerical Mathematics*, **7**:105–131, 1999.

[33] L. Formaggia and F. Nobile. Stability analysis of second-order time accurate schemes for ALE-FEM. *Computer Methods in Applied Mechanics and Engineering*, **193**:4097–4116, 2004.

[34] L. Forti and L. Dedè. Semi-implicit BDF time discretization of the Navier-Stokes equations with VMS-LES modeling in a High Performance Computing framework. *Computers & Fluids*, **117**:168–182, 2015.

[35] V. Gravemeier, A. Comerford, L. Yoshihara, M. Ismail, and W. Wall. A novel formulation for Neumann inflow boundary conditions in Biomechanics. *International Journal for Numerical Methods in Biomedical Engineering*, **28**:560–573, 2012.

[36] B.O. Haugen, S. Berg, K.M. Brecke, S.O. Samstad, S.A. Slørdahl, T. Skjærpe, and H. Torp. Velocity profiles in mitral blood flow based on three-dimensional freehand colour flow imaging acquired at high frame rate. *European Journal of Echocardiography*, **1**:252–256, 2000.

[37] J.G. Heywood, R. Rannacher, and S. Turek. Artificial boundaries and flux and pressure conditions for the incompressible Navier-Stokes equations. *International Journal for numerical methods in fluids*, **22**:325–352, 1996.

[38] G.R. Hong, G. Pedrizzetti, G. Tonti, P. Li, Z. Wei, J.K. Kim, A. Baweja, S. Liu, N. Chung, H. Houle, J. Narula, and M.A. Vannan. Characterization and quantification of vortex flow in the human left ventricle by contrast echocardiography using vector particle image velocimetry. *JACC: Cardiovascular Imaging*, **1**:705–717, 2008.

[39] M.-C. Hsu, I. Akkerman, and Y. Bazilevs. Wind turbine aerodynamics using ALE–VMS: validation and the role of weakly enforced boundary conditions. *Computational Mechanics*, **50**:499–511, 2012.

[40] M.-C. Hsu, D. Kamensky, Y. Bazilevs, M.S. Sacks, and T.J.R. Hughes. Fluid-structure interaction analysis of bioprosthetic heart valves: significance of arterial wall deformation. *Computational Mechanics*, **54**:1055–1071, 2014.

[41] J.C.R. Hunt, A.A. Wray, and P. Moin. Eddies, stream, and convergence zones in turbulent flows. *Center for Turbulence Research Report*, **CTR-S88**:193–208, 1988.

[42] D. Kamensky, M.-C. Hsu, D. Schillinger, J.A. Evans, A. Aggarwal, Y. Bazilevs, M.S. Sacks, and T.J.R. Hughes. An immersogeometric variational framework for fluid-structure interaction: Application to bioprosthetic heart valves. *Computer Methods in Applied Mechanics and Engineering*, **284**:1005–1053, 2015.

[43] K.E. Jansen, C.H. Whiting, and G.M. Hulbert. A generalized-α method for integrating the filtered Navier-Stokes equations with a stabilized finite element method. *Computer Methods in Applied Mechanics and Engineering*, **190**:305–319, 2000.

[44] M. Juntunen and R. Stenberg. Nitsche's method for general boundary conditions. *Mathematics of Computation*, **78**:1353–1374, 2009.

[45] M. Kanski, P.M. Arvidsson, J. Töger, R. Borgquist, E. Heiberg, M. Carlsson, and H. Arheden. Left ventricular fluid kinetic energy time curves in heart failure from cardiovascular magnetic resonance 4D flow data. *Journal of Cardiovascular Magnetic Resonance*, **17:111**:1–10, 2015.

[46] S.S. Khalafvand, E.Y.K. Ng, L. Zhong, and T.K. Hung. Fluid-dynamics modelling of the human left ventricle with dynamic mesh for normal and myocardial infarction: preliminary study. *Computers in Biology and Medicine*, **42**:863–870, 2012.

[47] P.J. Kilner, G.-Z. Yang, A.J. Wilkes, R.H. Mohiaddin, D.N. Firmin, and M.H. Yacoub. Asymmetric redirection of flow through the heart. *Nature*, **404**:759–761, 2000.

[48] H.J. Kim, C.A. Figueroa, T.J.R. Hughes, K.E. Jansen, and C.A. Taylor. Augmented Lagrangian method for constraining the shape of velocity profiles at outlet boundaries for three-dimensional finite element simulations of blood flow. *Computer Methods in Applied Mechanics and Engineering*, **198**:3551–3566, 2009.

[49] H.B. Kim, J.R. Hertzberg, and R. Shandas. Development and validation of echo PIV. *Experiments in Fluids*, **36**:455–462, 2003.

[50] W.Y. Kim, P.G. Walker, E.M. Pedersen, J.K. Poulsen, S. Oyre, K. Houlind, and A.P. Yoganathan. Left ventricular blood flow patterns in normal subjects: a quantitative analysis by three-dimensional magnetic resonance velocity mapping. *Journal of the American College of Cardiology*, **26**:224–238, 1995.

[51] S.J. Kovács, D.M. Mcqueen, and C.S. Peskin. Modelling cardiac fluid dynamics and diastolic function. *Philosophical Transactions of the Royal Society A.*, **359**:1299–1314, 2001.

[52] S. Krittian, U. Janoske, H. Oertel, and T. Böhlke. Partitioned fluid-solid coupling for cardiovascular blood flow: left-ventricular fluid mechanics. *Annals of Biomedical Engineering*, **38**:1426–1441, 2010.

[53] A. Laadhari and A. Quarteroni. Numerical modeling of heart valves using resistive Eulerian surfaces. *International Journal for Numerical Methods in Biomedical Engineering*, **32**:1–29, 2016.

[54] R.M. Lang, M. Bierig, R.B. Devereux, F.A. Flachskampf, E. Foster, P.A. Pellikka, M.H. Picard, M.J. Roman, J. Seward, J. Shanewise, S. Solomon, K.T. Spencer, M. St.John Sutton, and W. Stewart. Recommendations for chamber quantification. *European Journal of Echocardiography*, **7**:79–108, 2006.

[55] J.D. Lemmon and A.P. Yoganathan. Computational model of left heart diastolic function with fluid-structure interaction. *Journal of Biomechanical Engineering*, **122**:297–303, 2000.

[56] J.O. Mangual, E. Kraigher-Krainer, A. De Luca, L. Toncelli, A. Shah, S. Solomon, G. Galanti, F. Domenichini, and G. Pedrizzetti. Comparative numerical study on left ventricular fluid dynamics after dilated cardiomyopathy. *Journal of Biomechanics*, **46**:1611–1617, 2013.

[57] D.M. Mcqueen and C.S. Peskin. Heart Simulation by an Immersed Boundary Method with Formal Second-order Accuracy and Reduced Numerical Viscosity. In *Mechanics for a New Millennium*, Eds. Springer, Netherlands, 429–444, 2002.

[58] J.R. Mitchell and J.-Jr Wang. Expanding application of the Wiggers diagram to teach cardiovascular physiology. *Advances in Physiology Education*, **38**:170–175, 2014.

[59] R. Mittal and J.H. Seo, V. Vedula, Y.J. Choi, H. Liu, H.H. Huang, S. Jain, L. Younes, T. Abraham, and R.T. George. Computational modeling of cardiac hemodynamics: Current status and future outlook. *Journal of Computational Physics*, **305**:1065–1082, 2016.

[60] M.E. Moghadam, Y. Bazilevs, T.-Y. Hsia, I.E. Vignon-Clementel, and A.L. Marsden. A comparison of outlet boundary treatments for prevention of backflow divergence with relevance to blood flow simulations. *Computational Mechanics*, **48**:277–291, 2011.

[61] J. Nitsche. Über ein Variationsprinzip zur Lösung von Dirichlet-Problemen bei Verwendung von Teilräumen, die keinen Randbedingungen unterworfen sind. *Abhandlungen aus dem Mathematischen Seminar der Universität Hamburg*, **36**:9–15, 1971.

[62] C.S. Peskin. Flow patterns around heart valves: a numerical method. *Journal of Computational Physics*, **10**:252–271, 1972.

[63] C.S. Peskin. Numerical analysis of blood flow in the heart. *Journal of Computational Physics*, **25**:220–252, 1977.

[64] C.S. Peskin and D.M. McQueen. A three-dimensional computational model of blood flow in the heart: I. Immersed elastic fibers in a viscous incompressible fluid. *Journal of Computational Physics*, **81**:372–405, 1989.

[65] A. Quarteroni. *Numerical Models for Differential Problems*. Springer–Verlag, Milan, 2014.

[66] A. Quarteroni, T. Lassila, S. Rossi, and R. Ruiz-Baier. Integrated Heart - Coupled multiscale and multiphysics models for the simulation of the cardiac function. *Computer Methods in Applied Mechanics and Engineering*, 2016.

[67] A. Quarteroni, A. Veneziani, and C. Vergara. Geometric multiscale modeling of the cardiovascular system, between theory and practice. *Computer Methods in Applied Mechanics and Engineering*, **302**:193–252, 2016.

[68] H. Reul, N. Talukder, and W. Muller. Fluid mechanics of the natural mitral valve. *Journal of Biomechanics*, **14**:361–372, 1981.

[69] P. Reymond, F. Merenda, F. Perren, D. Rufenacht, and N. Stergiopulos. Validation of a one-dimensional model of the systemic arterial tree. *American Journal of Physiological Heart Circulation Physiology*, **297**:H208–H222, 2009.

[70] G. Savaré. Parabolic problems with mixed variable lateral conditions: an abstract approach. *Journal of Pure and Applied Mathematics*, **76**:321–351, 1997.

[71] P.P. Sengupta, G. Pedrizzetti, P.J. Kilner, A. Kheradvar, T. Ebbers, G. Tonti, A.G. Fraser, and J. Narula. Emerging Trends in CV Flow Visualization. *JACC: Cardiovascular Imaging*, **5**:305–316, 2012.

[72] B.K. Shivamoggi and G.J.F. van Heijst. The Okubo-Weiss criteria in two-Dimensional Hydrodynamic and Magnetohydrodynamic flows. *arXiv:1110.6190*, 2015 .

[73] A. Tagliabue. Isogeometric Analysis for reduced fluid–structure interaction models in Haemodynamic applications. Master Degree Thesis, Università degli Studi dell'Insubria, Italy, 2012. `http://infoscience.epfl.ch/record/183031/files/thesis_tagliabue_2012.pdf`.

[74] A. Tagliabue. Mathematical and Numerical Modeling of Blood Flow in an Idealized Left Ventricle. PhD thesis, Politecnico di Milano, Department of Mathematics, 2016.

[75] A. Tagliabue, L. Dedè, and A. Quarteroni. Nitsche's method for parabolic partial differential equations with mixed time varying boundary conditions. *ESAIM: Mathematical Modelling and Numerical Analysis*, **50**:541–563, 2015.

[76] A. Tagliabue, L. Dedè, and A. Quarteroni. Fluid dynamics of an idealized left ventricle: the extended Nitsche's method for the treatment of heart valves as mixed time varying boundary conditions. *MATHICSE report*, 2015.

[77] K. Takizawa, Y. Bazilevs, and T.E. Tezduyar. Space-time and ALE-VMS techniques for patient-specific cardiovascular fluid-structure interaction modeling. *Archives of Computational Methods in Engineering*, **19**:171–225, 2012.

[78] C. Vergara. Nitsche's method for defective boundary value problems in incompressible fluid-dynamics. *Journal of Scientific Computing*, **46**:100–123, 2011.

[79] J.A. Vierendeels, K. Riemslagh, E. Dick, and P.R. Verdonck Computer simulation of intraventricular flow and pressure during diastole. *Journal of Biomechanical Engineering*, **122**:667–674, 2000.

[80] H. Watanabe, S. Sugiura, H. Kafuku, and T. Hisada. Multiphysics simulation of left ventricular filling dynamics using fluid-structure interaction finite element method. *Biophysical Journal*, **87**:2074–2085, 2004.

[81] C.H. Whiting. *Stabilized Finite Element methods for fluid dynamics using a hierarchical basis.* Master's thesis, Rensselaer Polytechnic Institute Troy, New York, 1999.

[82] X. Zheng, J.H. Seo, V. Vedula, T. Abraham, R. Mittal. Computational modeling and analysis of intracardiac flows in simple models of the left ventricle. *European Journal of Mechanics B/Fluids*, **35**:31–39, 2012.

MOX Technical Reports, last issues

Dipartimento di Matematica
Politecnico di Milano, Via Bonardi 9 - 20133 Milano (Italy)

13/2017   Gigante, G.; Vergara, C.
Optimized Schwarz Methods for circular flat interfaces and geometric heterogeneous coupled problems

14/2017   Bruggi, M.; Parolini, N.; Regazzoni, F.; Verani, M.
Finite Element approximation of an evolutionary Topology Optimization problem

12/2017   Gasperoni, F.; Ieva, F.; Barbati, G.; Scagnetto, A.; Iorio, A.; Sinagra, G.; Di Lenarda, A.
Multi state modelling of heart failure care path: a population-based investigation from Italy

11/2017   Ferro, N.; Micheletti, S.; Perotto, S.
Anisotropic Mesh Adaptation for Crack Propagation Induced by a Thermal Shock

10/2017   Pini, A.; Stamm, A.; Vantini, S.
Hotelling's T^2 in separable Hilbert spaces

09/2017   Antonietti, P.F.; Ferroni, A.; Mazzieri, I.; Paolucci, R.; Quarteroni, A.; Smerzini, C.; Stupazzin
Numerical modeling of seismic waves by Discontinuous Spectral Element methods

08/2017   Ambrosi, D.; Beloussov, L.V.; Ciarletta, P.
Mechanobiology and morphogenesis in living matter: a survey

06/2017   Ekin, T.; Ieva, F.; Ruggeri, F.; Soyer, R.
On the Use of the Concentration Function in Medical Fraud Assessment

07/2017   Cabassi A.; Pigoli D.; Secchi P.; Carter P.A.
Permutation tests for the equality of covariance operators of functional data with applications to evolutionary biology

05/2017   Menafoglio, A.; Hron, K.; Filzmoser, P.
Logratio approach to distributional modeling